

©2009

Christina Marie Mossaad

ALL RIGHTS RESERVED

THERMODYNAMIC DESIGN, CHARACTERIZATION, AND EVALUATION OF A
NANOCRYSTALLINE HYDROXYAPATITE COLLAGEN ALLOGRAFT
COMPOSITE

by

CHRISTINA MARIE MOSSAAD

A Dissertation submitted to the
Graduate School-New Brunswick
Rutgers, The State University of New Jersey
in partial fulfillment of the requirements

for the degree of

Doctor of Philosophy

Graduate Program in Materials Science and Engineering

written under the direction of

Professor Richard E Riman

and approved by

New Brunswick, New Jersey

[January, 2009]

ABSTRACT OF THE DISSERTATION

Thermodynamic Design, Characterization, and Evaluation of a Nanocrystalline

Hydroxyapatite Collagen Allograft Composite

by CHRISTINA MARIE MOSSAAD

Dissertation Director:
Professor Richard E Riman

There is a growing need for bone to be produced synthetically due to the rising rates of osteoporosis and decreasing levels of bone mineral density in the rapidly aging population of baby boomers. Bone is a complex composite material of hydroxyapatite and collagen built to withstand tremendous compressive and tensile loads. The inorganic phase can be synthesized by various techniques including sol-gel, phase transformation, hydrothermal, mechanochemical, chemical precipitation and precipitation in simulated body fluid. However, high temperatures, high pressures, extreme pH values, low yield, vigorous washing and long reaction times limit biological applications and processing with biological tissues such as allografts used in a manifold of medical applications. To address the gap in hydroxyapatite synthesis technology for these applications, the research was divided into three parts: thermodynamic modeling, powder characterization, and the application to allograft materials for in-vivo studies. The thermodynamic modeling contained in the first chapter investigated four precursor systems of interest and their fit or dissidence with the biomimetic paradigm proposed. The calcium acetate-potassium phosphate tribasic synthesis system was found to be the most robust and was thoroughly characterized in the second chapter, which revealed the particle size to be

below 10 nm, which is among the smallest recorded in literature. In addition, characterization in this size range proved difficult and an uphill crystalline to amorphous phase transition was observed when left in dry storage over 5 months. In the third chapter, an inherent precursor buffering system was employed and the adaptation of the technology to aseptic conditions was carried out in effort to mineralize allograft materials for an in-vivo ectopic athymic rat study. The study revealed that the nanoscale hydroxyapatite synthesized on the surface allowed increased wet-state fiber cohesivity, which caused a change in tissue response over the control allograft where the allograft produced chondrocytes-cartilage-rich tissue and the composite produced osteoblast-adipose-rich tissue resembling bone marrow. Overall the research was successful in establishing the utility of thermodynamic modeling in designing a biomimetic system that can be aseptically adapted to allograft and other bone-related technologies, which is a rising field in the forefront of medicine.

Acknowledgements and Dedication

This thesis is comprised of three separate chapters, each fully written by myself, but with intellectual and laboratory collaboration with the stated co-authors. Each chapter will be a self-standing article to be published in a high ranking journal related to the subject matter.

In addition to my co-authors, I would like to acknowledge other colleagues who helped and supported this research from conception through execution. The Riman group at Rutgers through the years including Phyllis Cassell, Janet Pescinski, Eugene Zlotnikov, David Babson, Jennifer Czerepinski, Daniel Haders, Anders Petersson, Tamar Andelman, Swanand Patil, Vahit Atakan, and Mei-Chee Tan has been a source of invaluable advice and feedback on research throughout the process. A special thank you is also in order for the members of my thesis committee who have helped read and revise these articles as well as provide advice on the research direction. Most of all, I'd like to thank Rik Riman for all his support, guidance, and intellectual data transfer over the past 4.5 years, you really have changed my life and the way I think, giving me a huge lead in the professional world.

This thesis is dedicated to my family, who has supported me and loved me through everything. To my mother and father, thank you for being there for me and raising me just as you did, I would not change a thing, I love you. To my sisters and brother, thank you for your long chats on the phone and comic relief when I took myself too seriously, I love you. And to my soul mate, Peter, thank you for everything, thank you for completing me and giving me every reason and motivation to be the best person I can, I love you. Most of all, thank you to God, with whom everything is possible.

Table of Contents

Title Page	
Abstract	ii
Acknowledgements and Dedication	iv
Table of Contents	v
Introduction	1
Chapter 1	
Thermodynamic Modeling and Biomimetic Evaluation of Current	
Hydroxyapatite Synthesis Approaches and Design.....	2
Chapter 2	
Anomalous Size-Induced Crystalline to Amorphous Uphill Phase	
Transformation of Hydroxyapatite Nanoparticles	38
Chapter 3	
Ectopic Osteoinductive Effects of Demineralized Bone	
Matrix/Hydroxyapatite Composites on Bone Formation Pathways	70
Conclusions	98
Appendix	99
Curriculum Vitae	107

Introduction

This thesis was organized into three separate chapters comprised of three free-standing journal articles. Each of the chapters list collaborators and have separate introductions, experimental procedures, results, discussions, and conclusions. References and figures are found at the end of each relevant chapter and an appendix for all extraneous, but relevant data are found at the end of the entire document with a brief explanation of its importance.

The overall research goal of this thesis was to find a room temperature, neutral pH hydroxyapatite synthesis method that could be applied to allograft materials for structural and osteoconductive purposes. The hypothesis was that the mineralization of the allograft scaffolds would change and improve the in-vivo osteoinductive response due to having a stronger, more stable implant material and an increased level of osteoconduction afforded by the hydroxyapatite addition. The first chapter outlined the thermodynamic modeling results in the pursuit of the proper precursor chemistry that could mineralize allograft collagen under mild conditions to add biological and fiber cohesivity improvements. The second chapter explored the materials characterization properties of the precipitation products of the most promising precursor chemistry, calcium acetate and potassium orthophosphate, and evaluated the resulting nanostructure. The third and final chapter documented the application of the mild precipitation of hydroxyapatite on allograft materials and further characterized them through traditional materials science methods as well as an in-vivo athymic rat model study conducted in collaboration with Osteotech, Inc.

Chapter 1

Thermodynamic Modeling and Biomimetic Evaluation of Current Hydroxyapatite Synthesis Approaches and Design

Christina Mossaad

Matthew Starr

Richard E Riman

Rutgers, The State University of New Jersey, Department of Materials Science and
Engineering, 607 Taylor Road, Piscataway, NJ 08854

1. Abstract

The objective of this paper is to present a hydroxyapatite synthesis biomimetic paradigm and evaluate 4 precursor systems against its criteria. Thermodynamic modeling was used as a method of evaluation and the system that best fit the paradigm was experimentally verified through synthesizing 6 different precursor ratios and characterizing the products through X-Ray diffraction. The $\text{Ca}(\text{C}_2\text{H}_3\text{O}_2)_2\text{-K}_3\text{PO}_4\text{-H}_2\text{O}$ system was found to best fit the paradigm and was effective in synthesizing hydroxyapatite over the entire yield diagram modeled. Based on the findings of this diagram and its verification, it is hypothesized that thermodynamics largely govern the synthesis of hydroxyapatite in all these systems, making these models a cornerstone for future exploration in this field.

2. Introduction

Hydroxyapatite ($\text{Ca}_5(\text{PO}_4)_3\text{OH}$ or $\text{Ca}_{10}(\text{PO}_4)_6(\text{OH})_2$) is an inorganic material that possesses a variety of potential applications in modern science. It has been used in chromatography,¹ corrosion resistant materials,² drug delivery,³ and most notably in bone implant coatings⁴ and composites⁵ due to its osteoconductive nature. There has been a shift toward adapting hydroxyapatite synthesis techniques to more closely resemble how it is made naturally in the human body, or in other words, a biomimetic process. However, the majority of synthetic methods in literature cannot be classified as an entirely biomimetic process even though they may yield biomimetic materials. Many variations of a definition of biomimetic materials have been postulated involving the use of simulated body fluid, proteins, or collagen to produce hydroxyapatite, but these fail to address the flaws in the starting chemical precursors and a biomimetic process.^{6,7,8}

While these perspectives on biomimesis (the art of mimicking natural phenomena) are important, the precursor design is no less crucial in finding a true biomimetic system that can produce hydroxyapatite in high yield. The vision of a biomimetic crystallization paradigm, or model, for the creation of a less harsh hydroxyapatite synthesis method necessitates a critical look at the reaction conditions under which the mineral is formed naturally in the body. Average healthy body conditions are 37°C, pH of 7.4, which produce 10-40 nm hydroxyapatite crystals in hard tissue depending on mechanical loading, health, and nutrition.^{9,10,11} In contrast, current hydroxyapatite synthesis methods utilize reaction conditions from 25-1200 °C, pH of 8-12 (with or without a pH agent modification), producing particles anywhere from 15 nm to 2 μm .¹²⁻³³

A paradigm biomimetic hydroxyapatite synthesis system would precipitate at or below 37°C, relatively constant neutral pH (7-7.8), in high enough yield (>1 g per 100 mL reaction) for industrial applications in less than 4 h using precursors that do not leave toxic ions in solution. The ions left in solution should either be abundant in the body or metabolizable so minimum washing of the powder would be necessary prior to application. The pH could be controlled through the use of benign biological buffers or through the use of inherent precursor design. A synthesis time under 4 h is desirable because longer than this is not optimal for industrial scale up, could compromise aseptic processing in the manufacture of implant composites, and would not be optimal for surgical settings. A paradigm biomimetic precursor system could also mineralize live tissue during operative surgical procedures, an application that emphasizes the need for a short time and benign processing condition with high enough yield to produce a positive cellular response, but does not require specialized equipment or manipulation or washing after crystallization. A chemically robust system is one that does not entirely depend on input reactant stoichiometry (Ca/P range 0.5-4 and still produces HA) . Additionally having no dependency on the degree of mixing in both industrial and surgical venues would more easily yield consistent results, reducing concern of under/over mixing.

It is clear that current hydroxyapatite synthesis methods do not meet all these requirements in various ways. Methods commonly employed include mechanochemical^{12,13}, hydrothermal^{14,15,16,17}, sol-gel^{18,19,20,21}, precipitation^{22,23,24,25,26,27}, phase transition^{28,29,30}, and simulated body fluid^{31,32,33} crystallizations. The most widely used method is hydrothermal synthesis, which typically requires a long reaction time (> 24 h), high temperatures (50-300 °C) and high pressures (> 4 atm) to produce

hydroxyapatite, which are completely incompatible processing conditions for biological systems. Hydrothermal synthesis can be adapted to precipitate at room temperature and atmospheric pressure, but extreme pH is required, also prompting biological protein denaturation and degradation. Mechanochemical synthesis requires the use of high shear rates that would tear and break down any soft biological matter present. Sol-gel synthesis requires a solid state thermal treatment at high temperatures ($> 900\text{ }^{\circ}\text{C}$) to crystallize precursor powder, conditions yet again provoking breakdown of biological matter. The phase transition approach often requires the use of high pH (> 8) and long processing times ($> 24\text{ h}$) and high temperatures ($> 60\text{ }^{\circ}\text{C}$) to attain complete conversion. The use of simulated body fluid has become the most popular method of biomimesis, although the process is biomimetic, it has a fatal flaw in the innate long reaction time ($> 7\text{ days}$) and low yield ($\ll 0.1\text{ g per }100\text{ mL reaction}$), not conducive to application outside of research. Additionally, these methods often employ additional additives such as chelating agents and surfactants, which are necessary to remove prior to any biological exposure because of their toxicity.

The empirical, non-predictive, approaches used for hydroxyapatite synthesis have an opportunity for improvement through the use of thermodynamic modeling. Thermodynamic modeling has previously been used in designing successful synthesis approaches in lead titanate^{34,35} and perovskites.³⁶ By modeling hydroxyapatite solution synthesis, simple precursor inflows can be designed into the system and secondary reaction additives such as pH agents, surfactants, and chelating agents and their effects can be eliminated. It will also help explore modifications to systems in the literature so they can better fit the biomimetic paradigm. Many calcium and phosphate precursor

combinations have been used in solution precipitation of hydroxyapatite, however many of the individual precursors can be eliminated based on chemistry and their failure to fit the biomimetic paradigm. Ions that are the most prevalent in human blood plasma are Na^+ , Cl^- , and K^+ (142, 103, and 5 mmol/dm³, respectively).³⁷ Precursor design should take this into account, eliminating the use of iodides, hydroxides, nitrates and fluorides to name a few.

Three precursor systems that are widely used in literature to synthesize hydroxyapatite via solution precipitation at room temperature are $\text{CaCl}_2\text{-Na}_3\text{PO}_4$ ³⁸, $\text{CaCl}_2\text{-K}_2\text{HPO}_4$ ^{39,40,41,42}, and $\text{Ca(OH)}_2\text{-H}_3\text{PO}_4$.^{43,44,45} All have experimentally used a caustic agent to maintain a pH above 9 throughout the reaction, but through the use of thermodynamic modeling, it may be possible to find reaction conditions that adhere to the biomimetic paradigm. Following this paradigm further, this analysis will also omit surfactants, chelating agents, and other additives typically used for the above referenced works but not found in biological systems. Excluding these components and their potential thermodynamic effects also allows comparisons between the individual precursor systems. The CaCl_2 systems give information about how the precursor interacts with two different phosphate sources while the $\text{CaCl}_2\text{-Na}_3\text{PO}_4$ and $\text{Ca(OH)}_2\text{-H}_3\text{PO}_4$ systems may show the effects of using an orthophosphate source. In addition to these previously published chemistries, the $\text{Ca(C}_2\text{H}_3\text{O}_2)_2\text{-K}_3\text{PO}_4$ system models will be presented because it has not previously been investigated experimentally in the literature and will give additional comparisons for an orthophosphate model (it is analogous to Na_3PO_4) and its interactions with a highly soluble calcium precursor. Acetates are not native to human blood plasma, however, it is a natural metabolite of alcohol found in the

blood stream, so it is considered to fit the biomimetic paradigm well. Precursor systems that were modeled are shown in Table 1. The aqueous equilibrium pHs of the precursor solutions also show the trend in forming hydroxyapatite over another phase based on chemical selection. At least one basic component is necessary to form hydroxyapatite, as pH typically drops during crystallization due to consumption of hydroxyl ions in solution. The use of a basic solution does not fit the biomimetic paradigm requirements, but a fast reaction that produces a neutral pH after 4 h will still be promising.

Current methods of solution precipitation of hydroxyapatite employ harsh precursors and conditions that limit their true biomimetic qualities. The objective of this paper is to investigate the thermodynamic models of these systems and how they may be exploited to improve biomimetic solution synthesis. A biomimetic paradigm has been outlined to set guidelines for the changes in the precursor design. Four hydroxyapatite synthesis systems will be thermodynamically modeled to evaluate their biomimetic potential. One of these 4 systems will be chosen for experimental verification based on the results of the thermodynamic modeling and its fit with the biomimetic paradigm. It is hypothesized that if thermodynamics govern the solution synthesis of hydroxyapatite, then the proposed simulation approach will prove effective in biomimetic process design.

3. Thermodynamic Computation

3.1 Design

Thermodynamic modeling methods used in this work have been previously described in detail.⁴⁶ The focus of these models, simulated using the OLI Stream Analyzer 2.0, will be to describe the relevant simulations and their relation to the

biomimetic paradigm proposed. The thermodynamic databases that were specified for these simulations were the public, geothermal, and ceramic databases within the stream analyzer 2.0 from OLI systems, Inc.⁴⁷

In the thermodynamic design of a biomimetic system, the main variable parameters that impact the model are related to precursor selection, stoichiometry, and temperature, all which affect pH. Temperature for modeling was fixed at 25°C, while the titrants used in the chemical stability diagrams were chosen as HNO₃ and KOH, which are not biomimetic, but acidic and basic inflows are necessary to generate this model, not necessarily for real experimentation. Precursor inflows were chosen and fixed (other than where noted) at 0.5 m calcium and 0.3 m phosphate to model the systems at a relatively concentrated reaction for high yield, but maintaining stoichiometric proportions of Ca/P=1.67. Precursor dependent equilibrium reactions that take place in the synthesis of hydroxyapatite are presented in Table 2. All aqueous and solid species are labeled with an (aq) or an (s), while the ionic species show the corresponding charge.

Four types of diagrams were used to evaluate each of the precursor systems and fully explore their potential in the biomimetic paradigm. For each of the phase equilibrium systems explored, stability (a) and yield diagrams (b) along with temperature (c) and composition (d) surveys were generated. Across all diagrams, the shaded region indicates a 99% yield of hydroxyapatite and the incipient precipitation boundary of hydroxyapatite is shown with a solid line. Any aqueous or ionic species present is denoted with a dotted line, while secondary phase fields are shown with a dashed or dash-dot line.

The stability diagram shown in all figures as X.(a) correlates equilibrium pH versus log molal concentration ratio ($\text{Ca/P}=1.67$), which is effective in showing how equilibrium variable pH affects phase stability at a fixed precursor ratio. Yield is also shown with a shaded region on the diagram for a single selected phase, which in this case is hydroxyapatite. Temperature is fixed at 25°C for consistency among all diagrams and with the biomimetic paradigm.

The yield diagram X.(b) shows phase fields produced at different precursor inflow ratios of phosphate versus calcium in molal concentrations at a fixed temperature (25°C). The shaded region indicates a 99% yield of hydroxyapatite precipitate. The temperature and composition surveys that are also presented have been mapped on this yield diagram as a point (c) for temperature survey conditions and line (d) for composition survey conditions.

The temperature survey (c) shows phase output, theoretical output yield in moles, and equilibrium pH across the specified temperature range ($25\text{-}60^{\circ}\text{C}$), which is within reasonable limits of the biomimetic paradigm. This survey summarizes the changes in the yield diagram at a set point over a temperature range with additional quantitative yield and pH information. The precursor concentrations in all temperature surveys were conducted at $0.5/0.3\text{ m}$ ($\text{Ca/P}=1.67$). The phases that are produced at 25°C are directly shown within the corresponding phase field on the yield diagram (labeled point (I) on Figure X(b)).

The composition survey (d) shows the phase output, theoretical yield, and pH with variable phosphate concentration ($0\text{-}1\text{ m}$) at a fixed calcium concentration (0.5 m unless otherwise indicated). This is a re-representation of the yield diagram, but with

quantitative yield and pH at the set calcium concentration. The shown dominant phase changes on the composition survey are directly a result of crossing incipient precipitation boundaries on the yield diagram as labeled line (II) in figure X(b).

A general way to read each set of figures is to start with the stability diagram to target the desired phase to be synthesized, in this case hydroxyapatite, and the pH/solution concentration boundaries of the phase field. For the biomimetic paradigm, this would be a pH between 6.8 and 7.6. Since the stability diagram requires simulated titration of an acid and base, mentioned earlier, to generate the model, the true equilibrium solution pH can be mapped directly to the temperature survey (c) at 25°C. Depending on precursor selection, this pH range may or may not fall within the hydroxyapatite incipient precipitation boundary on the stability diagram (a). Next, reference the yield diagram and point (I) that corresponds to the conditions modeled in temperature survey (c), taking note how far inside the phase field the fixed Ca/P precursor ratio falls. The span of precursor ratios capable of producing hydroxyapatite is a measure of process robustness, in this case, it will be measured by an estimated proportion of the yield diagram covered with a shaded 99% hydroxyapatite yield. Synthesis process robustness is important when a process is scaled up to an industrial magnitude because all processes have some degree of experimental error for the precursor ratios, yet still produce the same product. Finally, referencing the composition survey (d) at the fixed 0.5 M calcium concentration shows and verifies the phases shown on the yield diagram along with the pH change seen as stoichiometry crosses the phase boundaries shown in the yield diagrams (b) along the composition survey line (II).

3.2 Thermodynamic Models

The $\text{CaCl}_2\text{-Na}_3\text{PO}_4\text{-H}_2\text{O}$, $\text{CaCl}_2\text{-K}_2\text{HPO}_4\text{-H}_2\text{O}$, $\text{Ca(OH)}_2\text{-H}_3\text{PO}_4\text{-H}_2\text{O}$, and $\text{Ca(C}_2\text{H}_3\text{O}_2)_2\text{-K}_3\text{PO}_4\text{-H}_2\text{O}$ precursor systems are shown in figures 1-4. The $\text{Ca(OH)}_2\text{-K}_3\text{PO}_4\text{-H}_2\text{O}$ and $\text{Ca(OH)}_2\text{-K}_2\text{HPO}_4\text{-H}_2\text{O}$ models are not presented because the final equilibrium pH of the systems was greater than 12 in both cases, eliminating them from consideration based on the biomimetic paradigm. The models using Na_3PO_4 are also not presented as they were close to identical to the same models presented that use K_3PO_4 .

Thermodynamic evaluation of each system will be based on temperature, pH, process synthesis robustness and yield parameters, systems not meeting the desired parameters will be eliminated from experimental verification. The phase pure precipitation of hydroxyapatite should happen between 20-40°C and a pH between 7 and 7.8 to be consistent with the biomimetic paradigm. Shaded area and corresponding process synthesis robustness should cover at least half the yield diagram indicating a large variation in composition will yield the same phase with no secondary phase contamination. Finally, the yield demonstrated in the composition survey should be at 99% yield of hydroxyapatite when the pH is in the targeted range of 7-7.8. The percent yield quoted for each system is calculated by taking the absolute moles of hydroxyapatite yielded on the composition survey when the pH is between 7 and 8 and dividing by the theoretical full yield of that system. The theoretical full yield is calculated by taking the molal quantity of calcium used in the composition diagram and dividing by 5 calcium ions used in each molecule of hydroxyapatite ($\text{Ca}_5(\text{PO}_4)_3\text{OH}$, used by this particular program), for most of the systems explored this is $0.5 \text{ molal}/5 = 0.1 \text{ moles}$.

3.2.1 $\text{CaCl}_2\text{-Na}_3\text{PO}_4\text{-H}_2\text{O}$ equilibria system

In the $\text{CaCl}_2\text{-Na}_3\text{PO}_4\text{-H}_2\text{O}$ system, two solid phases are shown to precipitate. Figure 1(a) shows a pH dependent precipitation of hydroxyapatite, the majority of this phase field occurring above pH 7. In the 0.5/0.3 m Ca/P ratio, the equilibrium pH at room temperature is about 6.2 (from figure 1(c)), making chloroapatite the dominant phase under the desired conditions when temperature is between 20-40°C. The yield diagram in figure 1(b) shows the co-precipitation of chloroapatite and hydroxyapatite in over half the area where calcium concentrations are equal to or higher than the phosphate concentration, corresponding to conditions when the pH is lower than 10. The phase pure hydroxyapatite phase field occurs in the other half, dominantly where the system is in excess of phosphate ($\text{Ca/P} < 1.67$). Concentrating on these phase pure conditions in light of the biomimetic paradigm, the concentration survey shows the dominant hydroxyapatite precipitation occurs above a phosphate concentration of 0.35 m (calcium concentration of 0.5 m). This coincides with an equilibrium pH increase to over 8, which is outside the ideal biomimetic range. Precipitating very close to the single/double phase field boundary would target the pH to the proper range between 6.5 and 8, however it would limit the robustness of the system to where the phosphate precursor concentration could not fluctuate below 0.3 m when the calcium precursor concentration is kept at 0.5 m. Additionally, when the pH is kept in this range, the yield of hydroxyapatite is 99% but a slight change in composition will precipitate chloroapatite. Calculated yield is 76% which corresponds to a calcium concentration of 0.5 m and a phosphate concentration of 0.35 molal which yields a pH of 8. These secondary phase precipitation and lower yield

limitations indicate this system is not a good fit for the biomimetic paradigm, eliminating it as a candidate for experimental verification.

3.2.2 $\text{CaCl}_2\text{-K}_2\text{HPO}_4\text{-H}_2\text{O}$ equilibria system

When examining the $\text{CaCl}_2\text{-K}_2\text{HPO}_4\text{-H}_2\text{O}$ models in Figure 2, it is evident that there is a limited hydroxyapatite phase stability field within this precursor system. The stability diagram in figure 2(a) shows a pH dependent behavior of hydroxyapatite precipitation with an additional chloroapatite phase field coinciding with monetite between a pH of 1-7, whereas hydroxyapatite is phase pure above 7. The temperature survey (Figure 2(c)) for the 0.5/0.3 m concentration yields no hydroxyapatite over the entire 20-60°C range due to the formation of acidic HCl species in solution driving the pH far below its stability of 6.5-12, prompting the formation of monetite and chloroapatite. The composition survey in Figure 2(d) conducted at 0.125 m CaCl_2 , where hydroxyapatite is stable, shows an increase in equilibrium pH to values close to 7 through the use of excess phosphate above 0.34 m. The lower calcium concentration (0.125 m) used in this composition survey was chosen so the survey line on the yield diagram would intersect the hydroxyapatite phase region of interest. The yield diagram in 2(b) further emphasizes the limited stoichiometry ranges for the synthesis of phase pure hydroxyapatite showing only a small shaded region (~20% of the total area) when the precursor system is kept in extreme excess of phosphate ($\text{Ca/P} \ll 1.67$, $\text{Ca} < 0.2$ m, $\text{PO}_4 > 0.25$ m). The resulting robustness of this system is very low, only producing high yield phase pure hydroxyapatite in a small number of stoichiometries. At these stoichiometries, the yield is 99%, which corresponds to a calcium precursor concentration

of 0.125 m and phosphate precursor concentration of 0.5 m, producing a pH of 7. Note how far the temperature survey point (a) is away from the hydroxyapatite phase stability region, emphasizing how drastically the stoichiometry has to be changed to yield the targeted phase. The low robustness of the system alone eliminates this as a candidate for further experimental investigation.

3.2.3 $\text{Ca}(\text{OH})_2\text{-H}_3\text{PO}_4\text{-H}_2\text{O}$ equilibria system

Moving away from chloride based chemistries, the investigation of the $\text{Ca}(\text{OH})_2\text{-H}_3\text{PO}_4\text{-H}_2\text{O}$ system (Figure 3) yields a different set of thermodynamic issues when looking for biomimetic adaptations to fit the paradigm. The stability diagram in figure 3(a) shows the same pH dependent behavior seen in the previous models indicating this phenomenon is not unique to the precursor systems employed. In each of the three systems explored so far, the shaded region dimensions span from pH of about 6.5 to 14 and $\log[m_{(\text{PO}_4)}=m_{(\text{Ca})}/1.6667]$ of -4.2 to 0. There is a change in the shape of the secondary monetite phase field, showing an overlap and co-precipitation with hydroxyapatite around a pH of 5.25. The yield diagram in figure 3(b) indicates no area where hydroxyapatite is the only dominant phase at 99% yield, simply because this precursor system has a Ca/P ratio of 1.6667 that falls just outside the shaded region adjacent to the monetite field on the stability diagram. When calculating percent yield from the composition survey, however it is found that 99% yield may exist with a calcium precursor inflow of 0.5 m and phosphate precursor inflow of 0.3 m corresponding to a pH of 8. However, any deviation away from this phosphate precursor concentration will co-precipitate an undesired phase. The small triangular area where temperature survey point

(a) is located on the yield diagram Figure 3(b) yields hydroxyapatite as the only phase precipitated, however it is obvious this system is very sensitive to precursor ratio changes. A shift of Ca/P above 1.75 or below 1.0 will yield a co-precipitation field, severely limiting the robustness of this system and carrying it outside the desired pH range. Although hydroxyapatite is the dominant phase at 0.5/0.3 m over the entire temperature range of 20-60°C in figure 3(c), the equilibrium pH, at 9.1, is above the ideal range. However, looking at the composition survey, using a slight excess of phosphate (Ca/P=1.55-1.65) may serve to target the initial pH in the biological range of 7.1-7.6, but this range must be maintained throughout synthesis as not to precipitate secondary phases in this narrow region of targeted phase stability. Based on low yield and lack of robustness when in accordance to the biomimetic paradigm, this system was eliminated from experimental verification.

3.2.4 $\text{Ca}(\text{C}_2\text{H}_3\text{O}_2)_2\text{-K}_3\text{PO}_4\text{-H}_2\text{O}$ equilibria system

In the currently unexplored $\text{Ca}(\text{C}_2\text{H}_3\text{O}_2)_2\text{-K}_3\text{PO}_4\text{-H}_2\text{O}$ system shown in Figure 4, some different thermodynamic characteristics are observed. The stability diagram shows the same pH sensitivity as the other chemistries explored, however it appears to have a slightly more narrow pH region starting at 7 rather than around 6.5, so further analysis was done to see how the shaded 99% yield phase field may move when stoichiometry is altered (Ca/P=1.47-1.6833) in this system. As shown in Figure 5(a), the shaded hydroxyapatite precipitation region recedes with a decrease in the phosphate precursor concentration (increase in Ca/P ratio), the largest area being with an excess of phosphate at 1.47 Ca/P ratio, or 0.34 m K_3PO_4 . It is likely that this receding phenomena is also

seen in the other chemistries as well. The yield diagram in figure 4(b) shows a protruding monetite phase field and its recession with higher temperatures, being completely eliminated by 40°C. It is predicted that even inside this phase field hydroxyapatite will be a dominant co-precipitate, making this the only diagram explored that can yield hydroxyapatite over the entire range of precursor ratios ($\text{Ca}=0.001\text{-}1\text{ m}$, $\text{PO}_4=0.001\text{-}1\text{ m}$). Using an excess of phosphate or an excess of calcium will yield phase pure hydroxyapatite outside this monetite co-precipitation field, however only an excess of phosphate will produce 99% yield and reach the targeted biomimetic pH range (mapped from figure 4(d)). When the same model is calculated at 37°C (Figure 5(b)), the monetite phase field retracts to a very small area produced at high concentrations of precursors. The 0.5/0.3 m temperature survey indicates hydroxyapatite is not phase pure at room temperature, but by 31°C, it is the dominant precipitate. The equilibrium pH is low for the application to a biological system, but the compositional survey indicates the increase of phosphate concentration to 0.39 m would target the equilibrium pH to 7.5 and produce phase pure hydroxyapatite at 99% yield. The robustness of the system could be considered comparable to that of the $\text{CaCl}_2\text{-Na}_3\text{PO}_4\text{-H}_2\text{O}$ system, however crossing out of the 99% yield shaded region in a phosphate-deficient formulation when the temperature is brought up to 37°C, hydroxyapatite is still a phase pure precipitate, giving this system an advantage. Even when compared at 25°C, the area of the monetite phase field in this system is much smaller to design around than the co-precipitating chloroapatite phase field in the $\text{CaCl}_2\text{-Na}_3\text{PO}_4\text{-H}_2\text{O}$ precursor system. Given the advantages in robustness and the smaller secondary co-precipitation phase field, this system was chosen for experimental model verification.

4. Experimental Verification

4.1 Procedure

Six points were chosen on the diagram presented in Figure 4(d), 3 within the monetite phase field, and 3 at other stoichiometries within the predicted phase pure hydroxyapatite field within and outside the region of 99% yield. The synthesis of the powder was carried out using calcium acetate hydrate (99%, Acros Organics, Morris Plains, New Jersey) and potassium phosphate tribasic monohydrate (96%, Acros Organics, Morris Plains, New Jersey) as received with no further purification or treatment. The concentrations of the precursor solutions tested are presented in Figure 6 and are expressed pre mixing, for example, an experimental 1.0 m solution of calcium acetate would be 0.5 m after mixing with corresponding equal volume phosphate solution. A stock solution of calcium acetate and a separate stock solution of potassium phosphate tribasic were made by dissolving the appropriate amount of precursor in DI water (deionized water, Milli-Q biocell with RiOs-S, Millipore Systems, Inc., Billerica, MA) and filtering through a 0.2 μm PES membrane Nalgene filter (566-0020). An equal volume (50 mL) of each solution was measured out and the phosphate solution was added to the calcium solution. The resulting viscous liquid was then stirred rigorously until the formed amorphous thixotropic slurry turned white and reduced in viscosity (about 30 seconds). This solution was aged for 4 hours, centrifuged (Avanti J-26XP, Beckman Coulter, Fullerton, CA), washed (where indicated with 150 mL DI water each cycle), shell frozen (Labconco, Kansas City, MO), freeze dried (Dura-Dry μP , FTS Systems, Inc., Stone Ridge, NY) and desiccated (Drykeeper, Sanplatec Corp, Osaka, Japan,

humidity 30%) until ready for characterization. Powders that were fired were subjected to a 900°C heat treatment for 2 h in air to verify complete reaction of the precursors and reagent concentrations (2 h ramp to 900°C, 2 h hold, 6 hour ramp down). Processing pH over the reaction time is presented in Figure 7 for comparison to predicted equilibrium pH at the various stoichiometries.

It is notable that even after 4 h, none of the stoichiometries have fallen as low as the predicted equilibrium pH in Figure 4(b). The drop in pH during HA synthesis can be attributed to the consumption of hydroxyl ions as the hydroxyapatite crystal yield increases. The significant decrease in pH with just 2 brief washing cycles indicates that to ensure phase purity in future studies with this chemistry, pH during post synthesis processing should be closely monitored or the powder should be washed in buffered solutions. The sample nomenclature used is as follows: as-prepared (AP), as-prepared heat treated (APHT), as-prepared washed (APW), as-prepared washed and heat treated (APWHT).

4.2 Characterization

The yield model presented previously for the $\text{Ca}(\text{C}_2\text{H}_3\text{O}_2)_2\text{-K}_3\text{PO}_4\text{-H}_2\text{O}$ system was verified and characterized via X-Ray Diffraction (XRD) (Siemens Xrystalloflex, 30 mA, 40 kV, $\text{CuK}\alpha$, 20-60°, 0.03 step, 2 s dwell). Jade 8.0 was used to aid in phase identification with PDF numbers 01-074-0566 (hydroxyapatite), 01-077-0128 (monetite), 97-002-2239 (calcium potassium phosphate (V) alpha), 01-070-0364 (M tricalcium phosphate, α -TCP), and 01-070-2065 (R tricalcium phosphate, β -TCP).

4.3 Results and Analysis

The results of the XRD verification are presented in Figures 8 and 9. The as-synthesized powders in both the washed and unwashed conditions (Figures 8 (a), 9 (a)) yielded hydroxyapatite as the dominant phase in most cases. Looking at each of the 6 points tested, 3 were predicted to produce phase pure hydroxyapatite (points 2-4) and 3 were predicted to produce hydroxyapatite and monetite co-precipitates (points 1, 5-6). All as-prepared powder produced hydroxyapatite as predicted, and only AP6 produced the predicted small contingent of monetite (26.6°). What appeared inconsistent with the diagrams was the final pHs of the as-prepared powders, possibly suggesting there is a kinetic time component that plays an integral part, as the pHs were significantly higher than predicted, but the reaction was stopped at 4 h, probably far before equilibrium was reached. AP2, although with a starting pH of 9.5, higher than the paradigm allows, was the only stoichiometry experimentally investigated that seemed to fit the biomimetic model post synthesis (pH=7.2) without the use of washing, additives, or buffers. With the use of an even more calcium-rich ratio, it may have an even lower starting pH (targeted in the range of 7.4) and a shorter reaction time, although a smaller yield, being outside the 99% shaded region.

Although the final synthesis pHs are still above the desired target, it is notable that 1-2 gentle washing cycles was enough to bring the pH of all but 1 down to the targeted pH range of 7-7.8. In experience, other chemical systems, such as those modeled here, due to the use of pH agents, required a minimum of 3 intense washing cycles, diluting the synthesis liquid volume by up to 10 fold each time, to begin a pH drop, giving the acetate system a considerable advantage over other precursor systems for

large scale production of hydroxyapatite. The only unexpected result was that after washing, APW2, an extremely phosphate-deficient formulation, it was phase converted into monetite. Although unexpected, this was consistent with pH/phase predictions in the stability diagram, associated with the solution pH dropping below 6.5 in the post washing step shown in Figure 7. This suggests it is imperative to monitor and control pH while washing these powders to maintain these materials as hydroxyapatite. It is extremely interesting to note that the model-predicted synthesis of hydroxyapatite over the entire diagram did hold true, emphasizing this chemistry has a much higher degree of robustness than any previously explored.

To determine the presence of incomplete crystallization and non-stoichiometric hydroxyapatite, heat treatments of 900°C for 2 hours were done on both washed and unwashed powders to observe any high temperature phase development. Upon heat treating the AP powders, all phases transformed into dominantly calcium potassium phosphate (V) alpha (KCP) with a small amount of hydroxyapatite except AP2, which remained hydroxyapatite with no detectable secondary phases, indicating this calcium rich ratio produces stoichiometric HA, while the others are all non-stoichiometric. KCP is a phase predicted to form at high temperatures in traditional ternary and binary diagrams using a calcium and phosphate with a potassium component.⁴⁸ It can be speculated that leaving the potassium ions on the surface of the particles adjusted phase stability of hydroxyapatite at high temperatures, prompting the crystal structure to incorporate a significant potassium contingent, but remaining hexagonal. Hydroxyapatite is known to incorporate large amounts of impurities, so it is expected with higher rates of diffusion at this high temperature for this phase to develop. It would be interesting to see

if a different cation doped calcium phosphate phase develops at high temperature when using an alternative tribasic phosphate source such as sodium orthophosphate or ammonium orthophosphate. Moreover, since tricalcium phosphate was not formed, it can be speculated that there was no amorphous phase left at the end of reaction. Two brief washing cycles with DI water (Figure 9 (a)) purged the system of potassium preventing any calcium potassium phosphate development upon heat treatment. There was an exception, however, with the previously mentioned monetite that developed in APW2 due to a pH drop, which caused a transformation upon firing into dominantly monoclinic α -TCP. The APW5 did, however, develop a small quantity of monetite or amorphous calcium phosphate during or following the washing cycles, which appears to have converted into a small contingent of hexagonal β -TCP with firing (30.7°). The other APWHTs appear to have some small degree of phase transformation to β -TCP and/or monetite, but a considerable portion of these samples remained hydroxyapatite, even upon heat treatment. The amounts of monetite seen in the APWHTs can be likely ascribed to the second washing cycle causing a drop in pH into the metastable range below 7.

5. Conclusions

Thermodynamics do govern a large portion of the solution synthesis of hydroxyapatite and is effective in biomimetic design over all chemistries explored. The calcium acetate-potassium orthophosphate system has the best utilization potential due to its robustness and ability to synthesize hydroxyapatite over the entire range of stoichiometries explored. A pH dependent and 99% yield behavior demonstrated in the stability diagrams appears to be universal when single calcium and single phosphate precursors are employed at a stoichiometric ratio of $\text{Ca/P}=1.6667$.

6. Acknowledgements

The authors would like to acknowledge NASA GSRP grant NNG04GO44H and the Rutgers-NSF IGERT DGE 0333196 for their generous funding of this research.

7. References

- ¹ M A Lawson, Z Xia, et al. (2006). "Refining the use of hydroxyapatite column chromatography to reveal differences in relative binding affinities of bisphosphonates." *Bone* 38(3)S1: 55-55.
- ² C Garcia, S Cere, et al. (2004). "Bioactive coatings prepared by sol-gel on stainless steel 316L." *Journal of Non-Crystalline Solids* 348: 218-224.
- ³ M P Ginebra, T Traykova, et al. (2006). "Calcium phosphate cements as bone drug delivery systems: A review." *Journal of Controlled Release* 113(2): 102-110.
- ⁴ M C Kuo, and S K Yen (2002). "The process of electrochemical deposited hydroxyapatite coatings on biomedical titanium at room temperature." *Materials Science and Engineering: C* 20(1-2): 153-160.
- ⁵ G Wei, P X Ma (2004). "Structure and properties of nano-hydroxyapatite/polymer composite scaffolds for bone tissue engineering." *Biomaterials* 25: 4749-4757
- ⁶ E Landi, A Tampieri, G Celotti, R Langenati, M Sandri, S Sprio (2005). "Nucleation of biomimetic apatite in synthetic body fluids: dense and porous scaffold development." *Biomaterials* 26(16): 2835-2845.
- ⁷ M Kikuchi, T Ikoma, S Itoh, HN Matsumoto, Y Koyama, K Takakuda, K Shinomiya, J Tanaka, (2004). "Biomimetic synthesis of bone-like nanocomposites using the

- self-organization mechanism of hydroxyapatite and collagen." *Composites Science & Technology* 64(6): 819-825.
- 8 P X Ma (2008). "Biomimetic materials for tissue engineering." *Advanced Drug Delivery Reviews* 60(2): 184-198.
 - 9 J Z Ilich and J E Kerstetter (2000). "Nutrition in Bone Health Revisited: A Story Beyond Calcium." *Journal of the American College of Nutrition* 19(6): 715-737.
 - 10 F H Silver, J W Freeman, et al. (2003). "Collagen self-assembly and the development of tendon mechanical properties." *Journal of Biomechanics* 36(10): 1529-1553.
 - 11 K S Katti (2004). "Biomaterials in total joint replacement." *Colloids and Surfaces B: Biointerfaces* 39(3): 133-142.
 - 12 W L Suchanek, P Shuk, et al. (2002). "Mechanochemical-hydrothermal synthesis of carbonated apatite powders at room temperature." *Biomaterials* 23(3): 699-710.
 - 13 C Shu, W Yanwei, L Hong, P Zhengzheng, Y Kangde (2005). "Synthesis of carbonated hydroxyapatite nanofibers by mechanochemical methods." *Ceramics International* 31(1): 135-138.
 - 14 Q Liao, G Xu, G Yin, D Zhou, C Zheng, X Li (2002). "Hydrothermal synthesis of nano-hydroxyapatite crystals." *Journal of Functional Materials* 33(3): 338-340.
 - 15 M Cao, Y Wang, C Guo, Y Qi, C Hu (2004). "Preparation of ultrahigh-aspect-ratio hydroxyapatite nanofibers in reverse micelles under hydrothermal conditions." *Langmuir* 20(11): 4784-4786.
 - 16 L Yan, Y Li, Z Deng, J Zhuang, X Sun (2001). "Surfactant-assisted hydrothermal synthesis of hydroxyapatite nanorods." *International Journal of Inorganic Materials* 3(7): 633-637.
 - 17 J Liu, X Ye, H Wang, M Zhu, B Wang, H Yan (2003). "The influence of pH and temperature on the morphology of hydroxyapatite synthesized by hydrothermal method." *Ceramics International* 29(6): 629-633.
 - 18 I Kim, P N Kumta (2004). "Sol-gel synthesis and characterization of nanostructured hydroxyapatite powder." *Materials Science & Engineering B-Solid State Materials for Advanced Technology* 111(2-3): 232-236.
 - 19 TA Kuriakose, SN Kalkura, M Palanichamy, D Arivuoli, K Dierks, G Bocelli, C Betzel (2004). "Synthesis of stoichiometric nano crystalline hydroxyapatite by ethanol-based sol-gel technique at low temperature." *Journal of Crystal Growth* 263(1-4): 517-523.
 - 20 Ramanan, S. R. and R. Venkatesh (2004). "A study of hydroxyapatite fibers prepared via sol-gel route." *Materials Letters* 58(26): 3320-3323.
 - 21 A Grandjean-Laquerriere, P Laquerriere, et al. (2006). "Influence of the zinc concentration of sol-gel derived zinc substituted hydroxyapatite on cytokine production by human monocytes in vitro." *Biomaterials* 27(17): 3195-3200.
 - 22 C Li-yun, Z Chuan-bo, H Jian-feng (2005). "Influence of temperature, [Ca²⁺], Ca/P ratio and ultrasonic power on the crystallinity and morphology of hydroxyapatite nanoparticles prepared with a novel ultrasonic precipitation method." *Materials Letters* 59(14-15): 1902-1906.
 - 23 A Afshar, M Ghorbani, N Ehsani, MR Saeri, CC Sorrell (2003). "Some important factors in the wet precipitation process of hydroxyapatite." *Materials & Design* 24(3): 197-202.

- 24 H Zhang, Y Wang, Y Yan, S Li (2003). "Precipitation of biocompatible hydroxyapatite whiskers from moderately acid solution." *Ceramics International* 29: 413-418.
- 25 A Wang, D Liu, et al. (2007). "Size-controlled synthesis of hydroxyapatite nanorods by chemical precipitation in the presence of organic modifiers." *Materials Science and Engineering: C* 27(4): 865-869.
- 26 C Liu, Y Huang, et al. (2001). "Kinetics of hydroxyapatite precipitation at pH 10 to 11." *Biomaterials* 22: 301-306
- 27 M R Saeri, A Afshar, M Ghorbani, N Ehsani, C C Sorrell (2003). "The wet precipitation process of hydroxyapatite " *Materials Letters* 57(24-25): 4064-4069.
- 28 J C Rendón-Angeles, K Yanagisawa, N Ishizawa, S Oishi (2000). "Conversion of Calcium Fluorapatite into Calcium Hydroxyapatite under Alkaline Hydrothermal Conditions." *Journal of Solid State Chemistry* 151(1): 65-72.
- 29 M Yoshimura, P Sujaridworakun, F Koh, T Fujiwara, D Pongkao, A Ahniyaz (2004). "Hydrothermal conversion of calcite crystals to hydroxyapatite." *Materials Science & Engineering C: Biomimetic Materials, Sensors & Systems* 24(4): 521-525.
- 30 S Jinawath, D Polchai, et al. (2002). "Low-temperature, hydrothermal transformation of aragonite to hydroxyapatite." *Materials Science and Engineering: C* 22(1): 35-39.
- 31 L-J Zhang, X-S Feng, et al. (2004). "Hydroxyapatite/collagen composite materials formation in simulated body fluid environment." *Materials Letters* 58(5): 719-722.
- 32 A C Tas (2000). "Synthesis of biomimetic Ca-hydroxyapatite powders at 37 C in synthetic body fluids." *Biomaterials* 21: 1429-1438.
- 33 D Bayraktar, A C Tas (1999). "Chemical Preparation of Carbonated Calcium Hydroxyapatite Powders at 37oC in Urea-Containing Synthetic Body Fluids." *Journal of the European Ceramic Society* 19: 2573-2579
- 34 S-B Cho, J-S Noh, et al. (2003). "Low temperature hydrothermal synthesis and formation mechanisms of lead titanate (PbTiO₃) particles using tetramethylammonium hydroxide: thermodynamic modelling and experimental verification." *Journal of the European Ceramic Society* 23(13): 2323-2335.
- 35 M M Lencka, and R E Riman (1993). "Synthesis of Lead Titanate: Thermodynamic Modeling and Experimental Verification." *Journal of the American Ceramic Society* 76(10): 2649-2659.
- 36 M M Lencka, and R E Riman (1994). "Hydrothermal synthesis of perovskite materials: Thermodynamic modeling and experimental verification." *Ferroelectrics* 151(1-4 P 1): 159-164.
- 37 T Kokubo, H Kushitani, S Sakka, T Kitsugi and T Yamamuro (1990) "Solutions able to reproduce in vivo surface-structure changes in bioactive glass-ceramic A-W", *Journal of Biomeica. Materials Research* 24: 721-734.
- 38 Y Liu, D Hou, G Wang (2004). "A simple wet chemical synthesis and characterization of hydroxyapatite nanorods." *Materials Chemistry and Physics* 86: 69-73.

- 39 Y Wang, S Zhang, et al. (2006). "Hydrothermal synthesis of hydroxyapatite nanopowders using cationic surfactant as a template." *Materials Letters* 60(12): 1484-1487.
- 40 F Wang, M-S Li, et al. (2006). "Synthesis and microstructure of hydroxyapatite nanofibers synthesized at 37 [deg]C." *Materials Chemistry and Physics* 95(1): 145-149.
- 41 Y-F Chou, W-A Chiou, et al. (2004). "The effect of pH on the structural evolution of accelerated biomimetic apatite." *Biomaterials* 25: 5323-5331.
- 42 W Feng, L Mu-Sen, L Yu-Peng, G Sheng-Song (2005). "Synthesis of nanocrystalline hydroxyapatite powders in stimulated body fluid." *Journal of Materials Science* 40: 2073- 2076.
- 43 R K Roeder, G L Converse, et al. (2006). "Kinetic Effects on Hydroxyapatite Whiskers Synthesized by the Chelate Decomposition Method." *Journal of the American Ceramic Society* 89(7): 2096-2104.
- 44 N Y Mostafa (2005). "Characterization, thermal stability and sintering of hydroxyapatite powders prepared by different routes." *Materials Chemistry & Physics* 94: 333-341.
- 45 R Kumar, K H Prakash, P Cheang, K A Khor (2004). "Temperature driven morphological changes of chemically precipitated hydroxyapatite nanoparticles." *Langmuir* 20(13): 5196-5200.
- 46 R Riman, W Suchanek, et al. (2002). "Hydrothermal Crystallization of Ceramics." *Annales de Chimica Scientia Materialia* 27(6): 15-36
- 47 <http://www.olisystems.com>
- 48 ACerS-NIST Phase Equilibria Diagrams CD-ROM version 3.0.1 (2004)

Figures

Table 1. Phase equilibrium systems considered for the biomimetic paradigm where H denotes hydroxyapatite is the dominant phase at the fixed conditions ($\text{Ca/P}=1.67$, $T=25^\circ\text{C}$) and N indicates hydroxyapatite was not the dominant phase at the fixed conditions.

Precursor (pH)	K_2HPO_4 (9.00)	H_3PO_4 (1.32)	$\text{Na}_3\text{PO}_4/\text{K}_3\text{PO}_4$ (12.13/12.24)
CaCl_2 (6.73)	N	N	H
$\text{Ca}(\text{OH})_2$ (12.39)	H	H	H
$\text{Ca}(\text{C}_2\text{H}_3\text{O}_2)_2$ (8.92)	N	N	H

Table 2. Relevant chemical equilibria for all common precursor systems in synthesizing hydroxyapatite

$\text{H}_2\text{O (l)} = \text{H}^+ + \text{OH}^-$	$\text{Ca}_3(\text{PO}_4)_2 \text{ (s)} = 3\text{Ca}^{2+} + 2\text{PO}_4^{3-}$
$\text{H}_2\text{O (g)} = \text{H}_2\text{O (l)}$	$\text{CaH}_2(\text{PO}_4)_2 \cdot \text{H}_2\text{O (s)} = \text{Ca}^{2+} + 2\text{H}_2\text{PO}_4^- + \text{H}_2\text{O}$
$\text{HNO}_3 \text{ (g)} = \text{HNO}_3 \text{ (aq)}$	$\text{CaH}_2(\text{PO}_4)_2 \text{ (s)} = \text{Ca}^{2+} + 2\text{H}_2\text{PO}_4^-$
$\text{HNO}_3 \text{ (aq)} = \text{H}^+ + \text{NO}_3^-$	$\text{CaH}_2\text{PO}_4^- = \text{Ca}^{2+} + \text{H}_2\text{PO}_4^-$
$\text{HCl (g)} = \text{HCl (aq)}$	$\text{CaHPO}_4 \cdot 2\text{H}_2\text{O (s)} = \text{Ca}^{2+} + \text{HPO}_4^{2-} + 2\text{H}_2\text{O}$
$\text{HCl (aq)} = \text{H}^+ + \text{Cl}^-$	$\text{CaHPO}_4 \text{ (aq)} = \text{Ca}^{2+} + \text{HPO}_4^{2-}$
$\text{Na}_2\text{HPO}_4 \cdot 12\text{H}_2\text{O (s)} = 2\text{Na}^+ + \text{HPO}_4^{2-} + 12\text{H}_2\text{O}$	$\text{Ca}(\text{OH})_2 \text{ (s)} = \text{Ca}^{2+} + 2\text{OH}^-$
$\text{Na}_2\text{HPO}_4 \cdot 2\text{H}_2\text{O (s)} = 2\text{Na}^+ + \text{HPO}_4^{2-} + 2\text{H}_2\text{O}$	$\text{CaOH}^+ = \text{Ca}^{2+} + \text{OH}^-$
$0.1\text{Na}_2\text{O (s)} + 0.2\text{H}^+ = 0.2\text{Na}^+ + 0.1\text{H}_2\text{O}$	$\text{CaPO}_4^- = \text{Ca}^{2+} + \text{PO}_4^{3-}$
$\text{NaC}_2\text{H}_3\text{O}_2 \cdot 3\text{H}_2\text{O (s)} = \text{Na}^+ + \text{C}_2\text{H}_3\text{O}_2^- + 3\text{H}_2\text{O}$	$\text{CaO (s)} + 2\text{H}^+ = \text{Ca}^{2+} + \text{H}_2\text{O}$
$\text{NaC}_2\text{H}_3\text{O}_2 \text{ (aq)} = \text{Na}^+ + \text{C}_2\text{H}_3\text{O}_2^-$	$\text{Ca}(\text{C}_2\text{H}_3\text{O}_2)_2 \cdot \text{H}_2\text{O (s)} = \text{Ca}^{2+} + 2\text{C}_2\text{H}_3\text{O}_2^- + \text{H}_2\text{O}$
$\text{NaC}_2\text{H}_3\text{O}_2 \text{ (s)} = \text{Na}^+ + \text{C}_2\text{H}_3\text{O}_2^-$	$\text{Ca}(\text{C}_2\text{H}_3\text{O}_2)_2 \cdot 2\text{H}_2\text{O (s)} = \text{Ca}^{2+} + 2\text{C}_2\text{H}_3\text{O}_2^- + 2\text{H}_2\text{O}$
$\text{NaOH} \cdot \text{H}_2\text{O (s)} = \text{Na}^+ + \text{OH}^- + \text{H}_2\text{O}$	$\text{Ca}(\text{C}_2\text{H}_3\text{O}_2)_2 \text{ (aq)} = \text{Ca}^{2+} + 2\text{C}_2\text{H}_3\text{O}_2^-$
$\text{NaOH (s)} = \text{Na}^+ + \text{OH}^-$	$\text{Ca}(\text{C}_2\text{H}_3\text{O}_2)_2 \text{ (s)} = \text{Ca}^{2+} + 2\text{C}_2\text{H}_3\text{O}_2^-$
$\text{Na}_2\text{HPO}_4 \cdot 7\text{H}_2\text{O (s)} = 2\text{Na}^+ + \text{HPO}_4^{2-} + 7\text{H}_2\text{O}$	$\text{CaC}_2\text{H}_3\text{O}_2^+ = \text{Ca}^{2+} + \text{C}_2\text{H}_3\text{O}_2^-$
$\text{Na}_2\text{HPO}_4 \text{ (s)} = 2\text{Na}^+ + \text{HPO}_4^{2-}$	$\text{Ca}_2\text{Cl}_2\text{O} \cdot 2\text{H}_2\text{O (s)} + \text{H}^+ = 2\text{Ca}^{2+} + 2\text{Cl}^- + \text{OH}^- + 2\text{H}_2\text{O}$
$\text{Na}_3\text{PO}_4 \cdot 1\text{H}_2\text{O (s)} = 3\text{Na}^+ + \text{PO}_4^{3-} + \text{H}_2\text{O}$	$\text{CaCl}_2 \cdot \text{H}_2\text{O (s)} = \text{Ca}^{2+} + 2\text{Cl}^- + \text{H}_2\text{O}$
$\text{Na}_3\text{PO}_4 \cdot 6\text{H}_2\text{O (s)} = 3\text{Na}^+ + \text{PO}_4^{3-} + 6\text{H}_2\text{O}$	$\text{CaCl}_2 \cdot 2\text{H}_2\text{O (s)} = \text{Ca}^{2+} + 2\text{Cl}^- + 2\text{H}_2\text{O}$
$\text{Na}_3\text{PO}_4 \cdot 8\text{H}_2\text{O (s)} = 3\text{Na}^+ + \text{PO}_4^{3-} + 8\text{H}_2\text{O}$	$\text{CaCl}_2 \cdot 4\text{H}_2\text{O (s)} = \text{Ca}^{2+} + 2\text{Cl}^- + 4\text{H}_2\text{O}$
$\text{Na}_3\text{PO}_4 \text{ (s)} = 3\text{Na}^+ + \text{PO}_4^{3-}$	$\text{CaCl}_2 \cdot 6\text{H}_2\text{O (s)} = \text{Ca}^{2+} + 2\text{Cl}^- + 6\text{H}_2\text{O}$
$\text{Na}_4\text{P}_2\text{O}_7 \cdot 10\text{H}_2\text{O (s)} = 4\text{Na}^+ + \text{P}_2\text{O}_7^{4-} + 10\text{H}_2\text{O}$	$\text{CaCl}_2 \text{ (aq)} = \text{CaCl}^+ + \text{Cl}^-$
$\text{Na}_5\text{P}_3\text{O}_{10} \cdot 6\text{H}_2\text{O} + 2\text{OH}^- = 4\text{Na}^+ + \text{P}_2\text{O}_7^{4-} + 10\text{H}_2\text{O}$	$\text{CaCl}_2 \text{ (s)} = \text{Ca}^{2+} + 2\text{Cl}^-$
$\text{Na}_5\text{P}_3\text{O}_{10} \text{ (s)} + 2\text{H}_2\text{O} = 5\text{Na}^+ + 3\text{PO}_4^{3-} + 4\text{H}^+$	$\text{CaCl}^+ = \text{Ca}^{2+} + \text{Cl}^-$
$\text{NaH}_2\text{PO}_4 \cdot \text{H}_2\text{O (s)} = \text{Na}^+ + \text{H}_2\text{PO}_4^- + \text{H}_2\text{O}$	$\text{Ca}(\text{NO}_3)_2 \cdot 3\text{H}_2\text{O (s)} = \text{Ca}^{2+} + 2\text{NO}_3^- + 3\text{H}_2\text{O}$
$\text{NaH}_2\text{PO}_4 \cdot 2\text{H}_2\text{O (s)} = \text{Na}^+ + \text{H}_2\text{PO}_4^- + 2\text{H}_2\text{O}$	$\text{Ca}(\text{NO}_3)_2 \cdot 4\text{H}_2\text{O (s)} = \text{Ca}^{2+} + 2\text{NO}_3^- + 4\text{H}_2\text{O}$
$\text{NaH}_2\text{PO}_4 \text{ (s)} = \text{Na}^+ + \text{H}_2\text{PO}_4^-$	$\text{Ca}(\text{NO}_3)_2 \text{ (s)} = \text{Ca}^{2+} + 2\text{NO}_3^-$
$\text{NaH}_2\text{PO}_4 \cdot 12\text{H}_2\text{O (s)} = 3.25\text{Na}^+ + \text{PO}_4^{3-} + .25 \text{OH}^- + 12\text{H}_2\text{O}$	$\text{CaNO}_3^+ \text{ (s)} = \text{Ca}^{2+} + \text{NO}_3^-$
$\text{K}_2\text{HPO}_4 \cdot 3\text{H}_2\text{O (s)} = 2\text{K}^+ + \text{HPO}_4^{2-} + 3\text{H}_2\text{O}$	$\text{Ca}_8\text{H}_2(\text{PO}_4)_6 \text{ (s)} = 4\text{Ca}^{2+} + \text{H}^+ + 3\text{PO}_4^{3-} + 2.5\text{H}_2\text{O}$
$\text{K}_2\text{HPO}_4 \cdot 6\text{H}_2\text{O (s)} = 2\text{K}^+ + \text{HPO}_4^{2-} + 6\text{H}_2\text{O}$	$\text{Ca}_5(\text{PO}_4)_3\text{OH (s)} = 0.5\text{Ca}^{2+} + 0.3\text{PO}_4^{3-} + 0.1\text{OH}^-$
$\text{K}_2\text{HPO}_4 \text{ (s)} = 2\text{K}^+ + \text{HPO}_4^{2-}$	$0.1\text{Ca}_5(\text{PO}_4)_3\text{Cl (s)} = 0.5\text{Ca}^{2+} + 0.3\text{PO}_4^{3-} + 0.1\text{Cl}^-$
$\text{K}_3\text{PO}_4 \cdot 3\text{H}_2\text{O (s)} = 3\text{K}^+ + \text{PO}_4^{3-} + 3\text{H}_2\text{O}$	$\text{P}_2\text{O}_7^{4-} + \text{H}_2\text{O} = 2\text{PO}_4^{3-} + 2\text{H}^+$
$\text{K}_3\text{PO}_4 \cdot 7\text{H}_2\text{O (s)} = 3\text{K}^+ + \text{PO}_4^{3-} + 7\text{H}_2\text{O}$	$\text{H}_2\text{P}_2\text{O}_7^{2-} = \text{H}^+ + \text{HP}_2\text{O}_7^{3-}$
$\text{K}_3\text{PO}_4 \text{ (s)} = 3\text{K}^+ + \text{PO}_4^{3-}$	$\text{H}_2\text{PO}_4^- = \text{H}^+ + \text{HPO}_4^{2-}$
$\text{KH}_2\text{PO}_4 \text{ (s)} = \text{K}^+ + \text{H}_2\text{PO}_4^-$	$\text{H}_3\text{P}_2\text{O}_7^- = \text{H}^+ + \text{H}_2\text{P}_2\text{O}_7^{2-}$
$\text{KC}_2\text{H}_3\text{O}_2 \text{ (aq)} = \text{K}^+ + \text{C}_2\text{H}_3\text{O}_2^-$	$\text{H}_3\text{P}_2\text{O}_7 \text{ (aq)} = \text{H}^+ + \text{H}_2\text{PO}_4^-$
$\text{KOH} \cdot \text{H}_2\text{O (s)} = \text{K}^+ + \text{OH}^- + \text{H}_2\text{O}$	$\text{H}_4\text{P}_2\text{O}_7 \text{ (aq)} = \text{H}^+ + \text{H}_3\text{P}_2\text{O}_7^-$
$\text{KOH} \cdot 2\text{H}_2\text{O (s)} = \text{K}^+ + \text{OH}^- + 2\text{H}_2\text{O}$	$\text{HP}_2\text{O}_7^{3-} = \text{H}^+ + \text{P}_2\text{O}_7^{4-}$
$\text{KC}_2\text{H}_3\text{O}_2 \text{ (s)} = \text{K}^+ + \text{OH}^-$	$\text{HPO}_4^{2-} = \text{H}^+ + \text{PO}_4^{3-}$
$0.1\text{K}_2\text{O (s)} + 0.2\text{H}^+ = 0.2\text{K}^+ + 0.1\text{H}_2\text{O}$	$0.1\text{P}_4\text{O}_{10} \text{ (s)} + 0.6\text{H}_2\text{O} = 0.4\text{H}_2\text{PO}_4^- + 0.4\text{H}^+$
$\text{KCl (aq)} = \text{K}^+ + \text{Cl}^-$	$(\text{C}_2\text{H}_3\text{O}_2)_2 \text{ (aq)} = 2\text{C}_2\text{H}_3\text{O}_2^- \text{ (aq)}$
$\text{KCl (s)} = \text{K}^+ + \text{Cl}^-$	$(\text{C}_2\text{H}_3\text{O}_2)_2 \text{ (g)} = (\text{C}_2\text{H}_3\text{O}_2)_2 \text{ (aq)}$
$\text{KNO}_3 \text{ (s)} = \text{K}^+ + \text{NO}_3^-$	$\text{CH}_3\text{COOH (aq)} = \text{H}^+ + \text{C}_2\text{H}_3\text{O}_2^-$
$\text{KOH (s)} = \text{K}^+ + \text{OH}^-$	$\text{CH}_3\text{COOH (g)} = \text{CH}_3\text{COOH (aq)}$

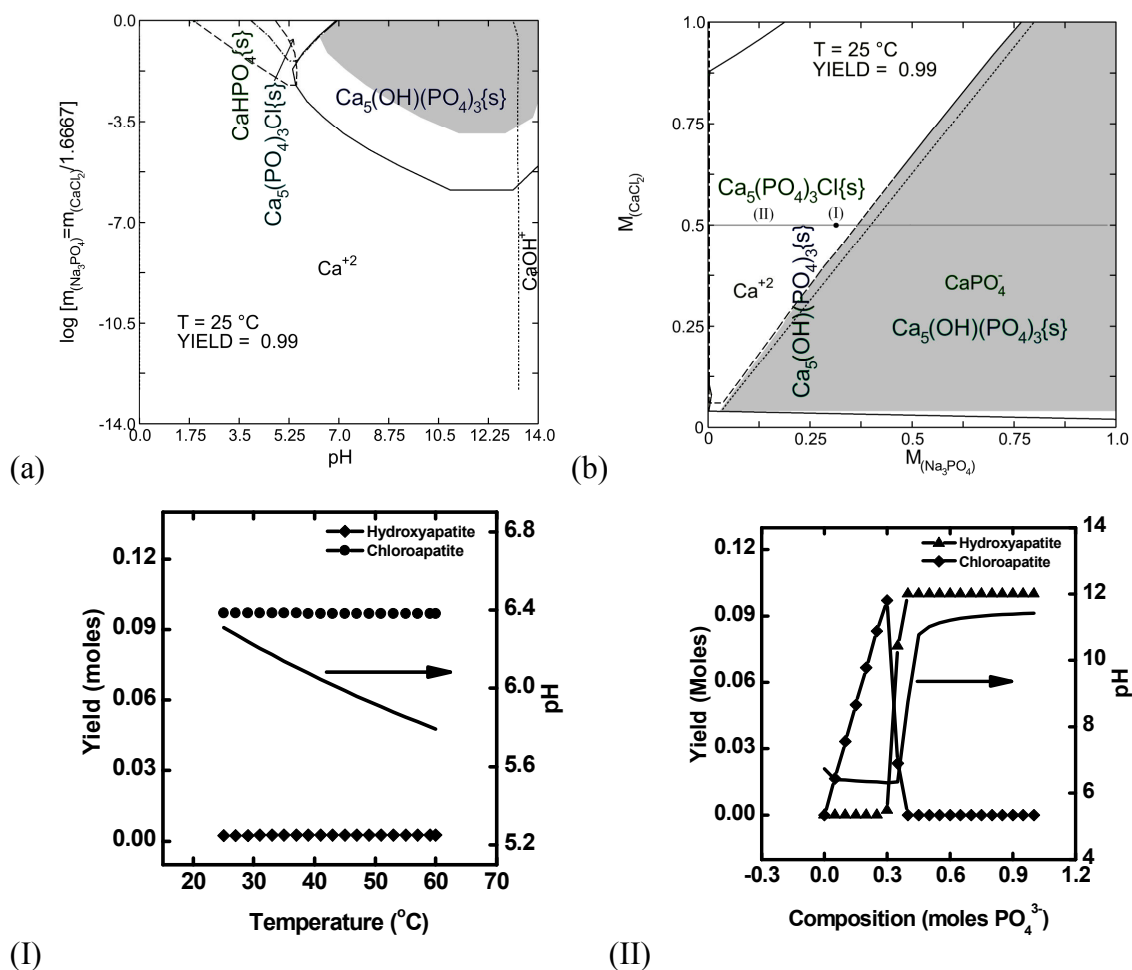


Figure 1. (a) Stability diagram (0.5 m CaCl_2 , 0.3 m Na_3PO_4) and (b) yield diagram with corresponding (I) point and (II) line of conditions surveyed. (I) Temperature survey at 0.5 m CaCl_2 , 0.3m Na_3PO_4 and (II) composition survey at 25°C , 0.125 m CaCl_2 .

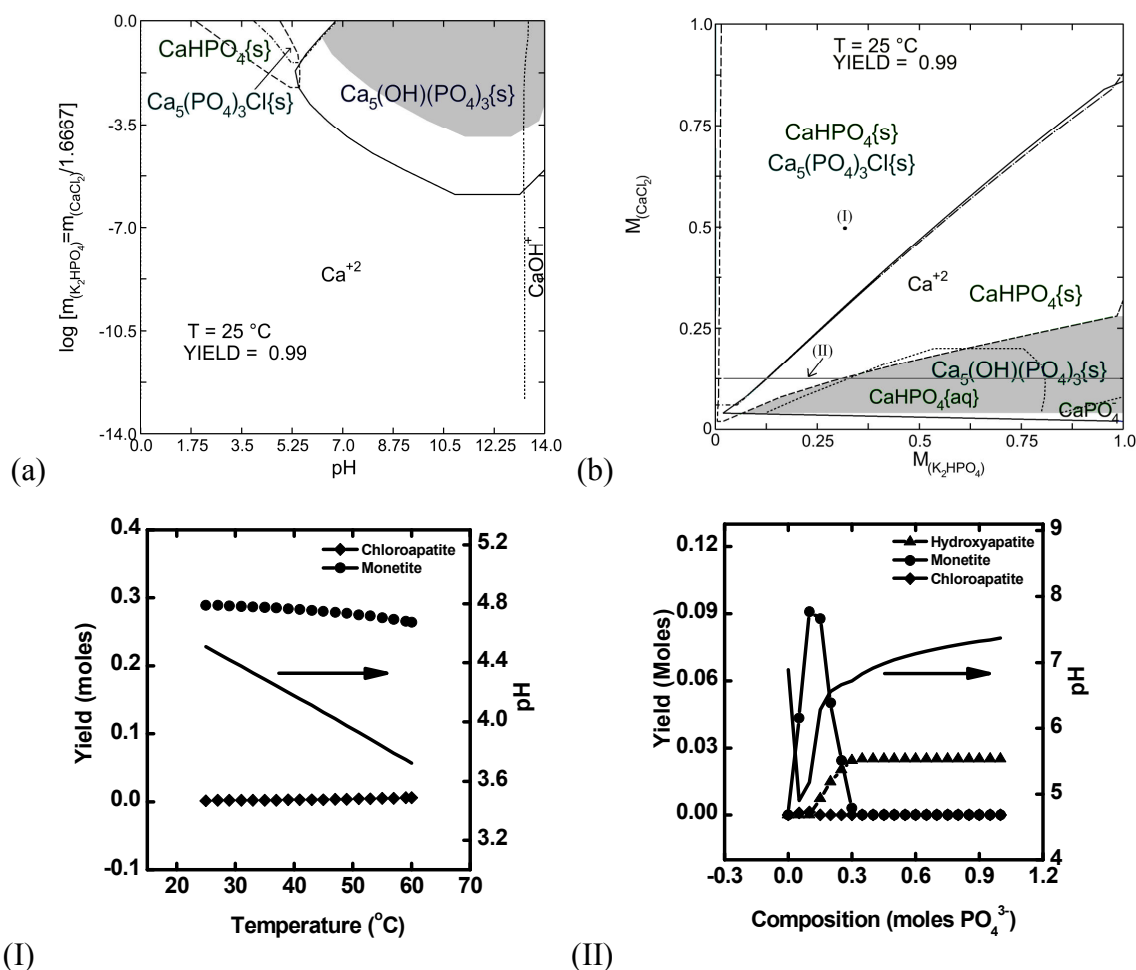


Figure 2. (a) Stability diagram (0.5 m $CaCl_2$, 0.3 m K_2HPO_4) and (b) yield diagram with corresponding (I) point and (II) line of conditions surveyed. (I) Temperature survey at 0.5 m $CaCl_2$, 0.3m K_2HPO_4 and (II) composition survey at 25°C , 0.125 m $CaCl_2$.

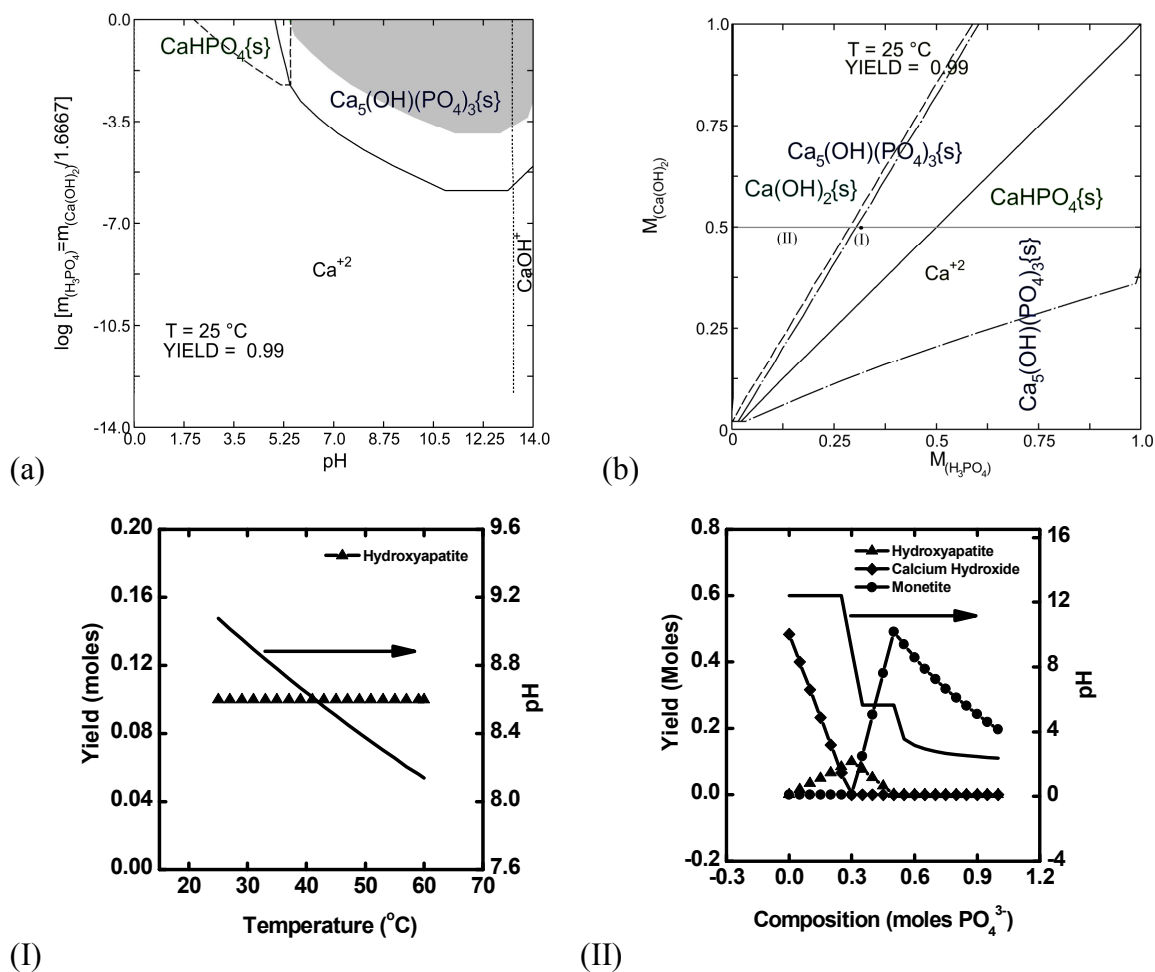


Figure 3. (a) Stability diagram (0.5 m Ca(OH)_2 , $0.3 \text{ m H}_3\text{PO}_4$) and (b) yield diagram with corresponding (I) point and (II) line of conditions surveyed. (I) Temperature survey at 0.5 m Ca(OH)_2 , $0.3 \text{ m H}_3\text{PO}_4$ and (II) composition survey at 25°C , 0.5 m Ca(OH)_2 .

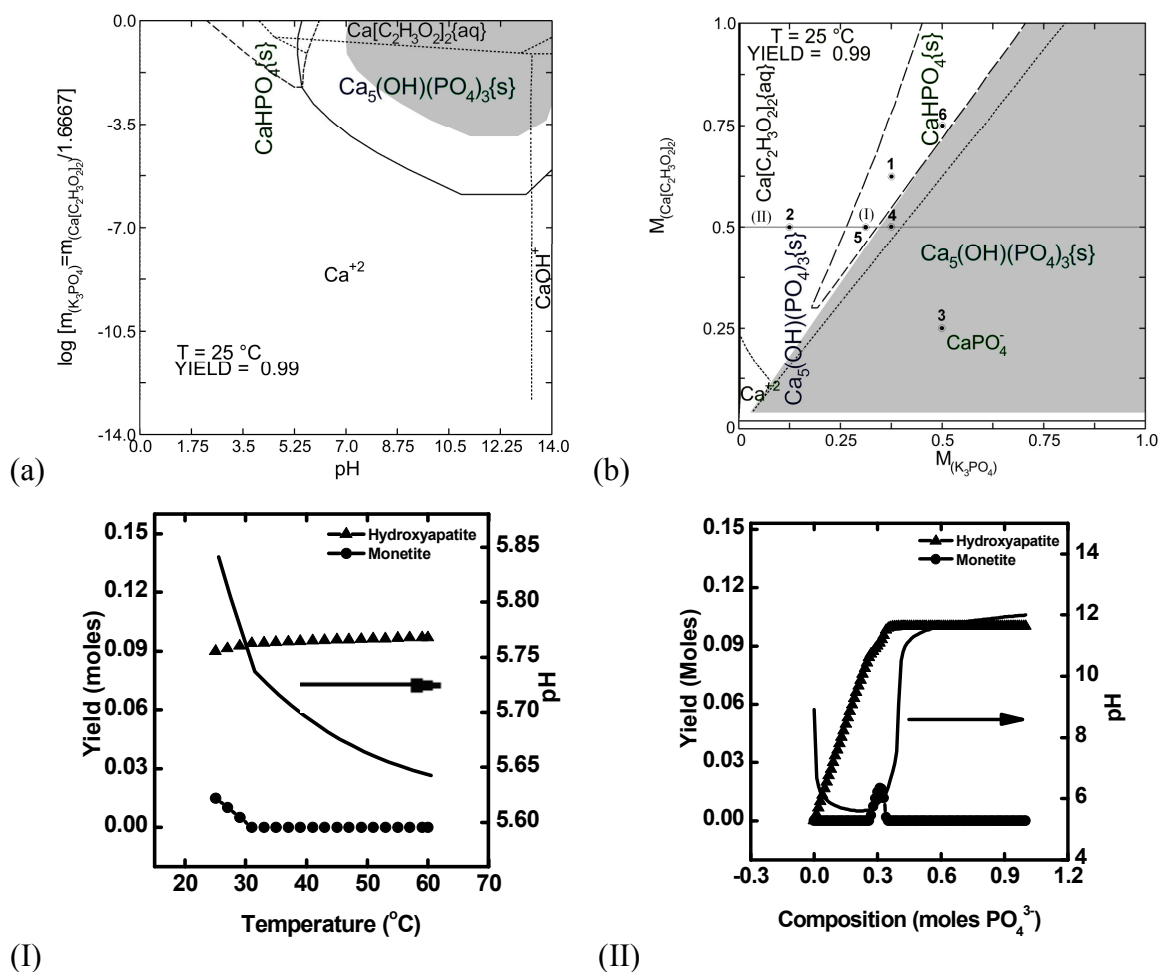


Figure 4. (a) Stability diagram (0.5 m $Ca(C_2H_3O_2)_2$, 0.3 m K_3PO_4) and (b) yield diagram with corresponding (I) point and (II) line of conditions surveyed and 1-6 points of verification. (I) Temperature survey at 0.5 m $Ca(C_2H_3O_2)_2$, 0.3 m K_3PO_4 and (II) composition survey at $25^\circ C$, 0.5 m $Ca(C_2H_3O_2)_2$

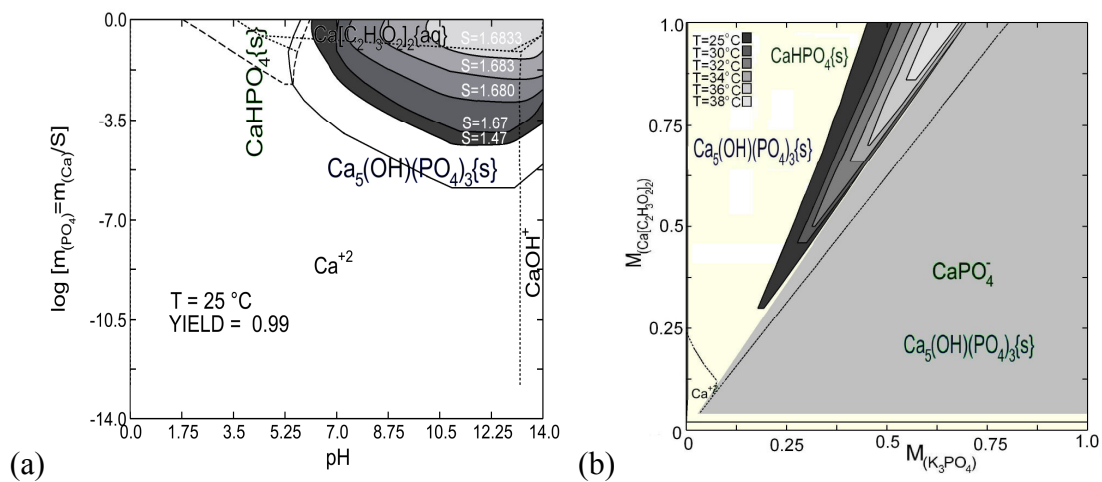


Figure 5. (a) Stability diagram with corresponding adjustments in stoichiometry and its effects on 99% yield area and (b) yield diagram at 37°C .

Table 3. Table of conditions (1-6) experimentally tested in figure 4 (d) and their respective compositions

Sample ID	Computed Ratio	Calcium SS (m)	Phosphate SS (m)	Solution Ca/P Ratios Post Mixing (m)
1	1.67	1.25	0.75	0.625 / 0.375
2	4.00	1.00	0.25	0.500 / 0.125
3	0.50	0.50	1.00	0.250 / 0.500
4	1.33	1.00	0.75	0.500 / 0.375
5	1.67	1.00	0.60	0.500 / 0.300
6	1.50	1.50	1.00	0.750 / 0.500

Table 4. Measured pH of conditions 1-6 throughout reaction time including solution pH after 2 washing cycles.

Sample ID						
Time (h)	1	2	3	4	5	6
0	11.0	9.5	14.0	10.0	11.0	12.0
1	9.5	9.0	14.0	10.0	9.0	9.5
2	9.5	8.5	14.0	10.0	9.0	9.5
3	9.0	7.2	14.0	9.5	9.0	9.5
4	8.5	7.2	14.0	9.5	9.0	9.0
Post wash (2 Cycles)	6.9	<6.5	12.0	7.2	6.9	6.9

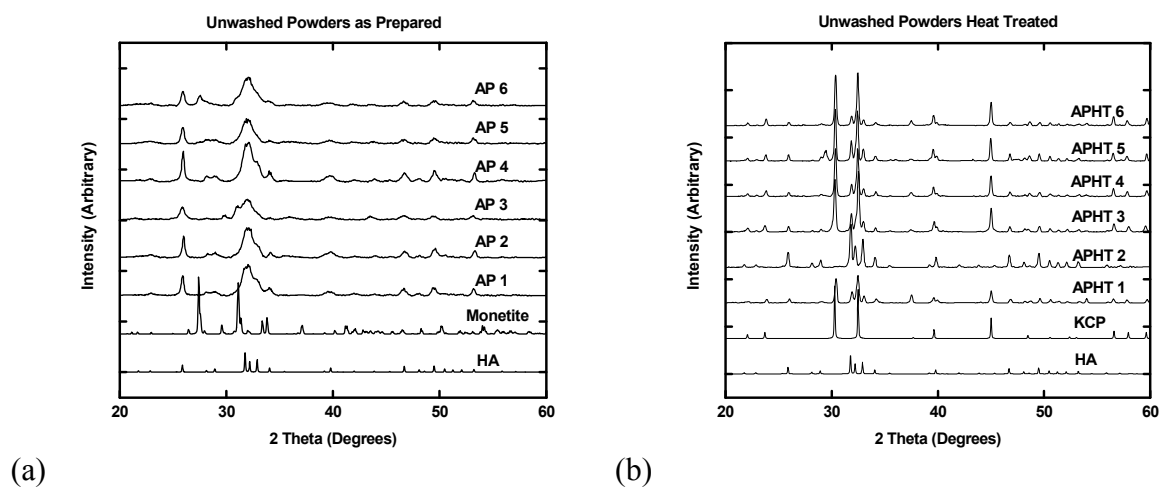


Figure 6. XRD of (a) unwashed powders as-synthesized, (b) unwashed fired powders showing a phase development of calcium potassium phosphate (V) alpha.

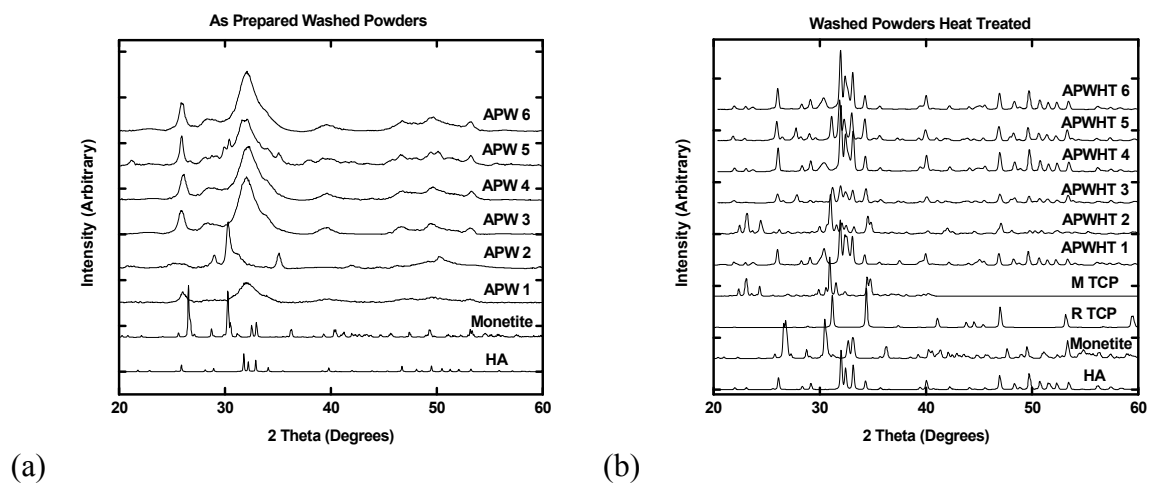


Figure 7. XRD of (a) washed powders, (b) washed fired powders demonstrating sensitive secondary phase developments that heavily rely upon washing treatments.

Chapter 2

**Anomalous Size-Induced Crystalline to Amorphous Uphill Phase Transformation of
Hydroxyapatite Nanoparticles**

Christina Mossaad ^a

Matthew Starr ^a

Andrew Payzant ^b

Jane Howe ^b

Richard E Riman ^a

^a Rutgers, The State University of New Jersey, Department of Materials Science and Engineering, 607 Taylor Road, Piscataway, NJ 08854

^b Oak Ridge National Laboratory, P.O. Box 2008, Oak Ridge, TN 37831

1. Abstract

The objective of the present paper was to produce nanoscale hydroxyapatite at room temperature under 10 nm through a simple method that requires no specialized equipment, surfactants, or additives. The $\text{Ca}(\text{C}_2\text{H}_3\text{O}_2)_2\text{-K}_3\text{PO}_4\text{-H}_2\text{O}$ synthesis system explored in previous literature was employed and the nanoscale powder product completely characterized through X-Ray Diffraction, Transmission Electron Microscopy, BET Nitrogen Surface area adsorption, Helium Pycnometry, TGA and Karl Fisher Titration. In accordance with other materials, it was found that hydroxyapatite under 5 nm produced by this chemistry undergoes an uphill phase transformation when left in dry storage over 5 months. Although it is possible to produce hydroxyapatite (and other materials) in this size range, it is imperative that care is taken through storage alterations to prevent any undesirable changes in structure or surface chemistry.

2. Introduction

As the average human life span increases, so does prevalence of health issues, making biomaterials an ever-present aspect of medicine and recovery. Stents are commonly used to widen coronary arteries that become blocked due to atherosclerosis, artificial pacemakers are used to keep the heart muscle contracting at a proper rate, and solid metallic implants are used in total joint replacement of the knee and hip to maintain locomotion of the body with significantly less pain for the patient. The technology must be continually improved to address issues that arise in degradation, encapsulation, and inflammation surrounding the device. Specifically with orthopedic implants, improvements must be made in mechanical properties, osteoconductivity, osteoinductivity, and the bioactivity of the implant-tissue interface formed. Using higher surface area materials and coatings may afford the needed improvements for better tissue interface integration.

Hydroxyapatite is often used as a coating on orthopedic devices for its osteoconductive properties and recently, on vascular implants for its drug delivery capabilities.¹ Hydroxyapatite, $\text{Ca}_{10}(\text{PO}_4)_6(\text{OH})_2$, is a hexagonal calcium orthophosphate with a significant chemical similarity to the inorganic mineral found in bone.² It has been widely accepted as osteoconductive,^{3,4} but there has also been literature speculating osteoinductive properties,⁵ however this has been continually under debate.⁶ Native bone apatite is found as platelets or rods with the largest dimensions in the range of 20-40 nm depending on local mechanical demands.^{7,8} However, the high yield, controlled size synthetic production of nanoscale hydroxyapatite in and below this size range has been a significant challenge.

Recently, hydroxyapatite synthesis has rapidly moved into the under-20 nm size range, affording multifaceted applications due to its inherent higher surface area properties and resulting increased cellular conductivity.⁹ In tissue engineering, it has been observed that micro- and especially nano-topography on surfaces has a significant effect on cell adhesion, induction, viability and prompting of maturation,^{9,10} strengthening the interfacial bond between host tissue and implant. Biomaterial intramuscular osteoinduction was also found to be enhanced with a higher specific surface area due to higher surface reactivity which would improve the cellular response in an implant site.¹¹ In addition to improved bone activity factors, nanoscale high surface area hydroxyapatite would also find increased value in drug delivery applications, but would require a robust process with high yield and closely controlled particle size.

Synthetic hydroxyapatite sizes in literature range from 8 to 100 nm, through the use of various, often harsh, techniques.^{12,13,14,15} Hydroxyapatite with surface area as high as 180 m²/g was hydrothermally synthesized for 8 h at 120°C, however the calculated particle size varied from 10 to 60 nm, with no HRTEM confirmation.¹⁶ Through the use of single and mixed surfactants, 8 to 20 nm lath-shaped hydroxyapatite particles were synthesized after 48 hours, yielding a surface area measurement of 364 m²/g.¹⁷ Although both methods successfully produced nano-hydroxyapatite, the equipment, procedural specificity, and long reaction time involved leave many variables that could alter the outcome (i.e. size and morphology) and may find difficulty in industrial scale-up due to these limitations. An instant continuous hydrothermal synthesis was recently explored, which would be more industrially ideal, yielding 15x65 nm rod agglomerates, however special equipment and temperatures of 200°C or more are needed.¹⁸ The technological

objective of the present paper is to meet and exceed these size ranges of HA (<10 nm) while optimizing synthesis procedures to be short and simplified, requiring no specialized equipment, extreme temperature or pressure conditions, or surfactant additives.

Pushing the lower limits of the hydroxyapatite synthesis size range presents some interesting material advantages. In the growing pursuit of biomimetic orthopedic structures, using building blocks of the same and smaller dimensions may allow for nanoscale assemblies closer to nature than previously observed. The higher surface area for functionalization may increase its utility as well, such as the case with carbon nanotubes and the manifold of applications and functionalizations it now employs. However, exploration and analysis of hydroxyapatite below 10 nm has not yet been fully explored or specifically predicted. Previous literature on other materials has proven phase transformations and metastability are common in this size range.

An uphill phase transition can be defined as one that goes against the thermodynamic stability prediction for a given bulk material. For many materials on the macroscale, a crystalline phase has a higher stability than a disordered amorphous phase based on free energy calculations; however, some materials are inherently non-crystalline and are generally classified as a glass. There are also polymorphic phase transitions where a particular crystal structure (cubic, tetragonal, monoclinic, etc.) has the highest stability at given conditions. In contrast, these general observations have not been seen in materials and structures below 10 nm due to unique surface-dominating properties. Surface free energy is typically neglected in continuum mechanics because it pertains to a few layers of surface atoms on a particle whose ratio is minute compared to the bulk volume properties.^{19,20} However when dealing with nanoparticles, this surface to volume

ratio is significantly higher, bringing to light the nanoscale behavior of a material. Dingreville et al. and Fischer et al. both studied the specific surface energy component adaptations to be included in continuum mechanics theory based on published literature on nanoparticles, nanobelts, nanowires, and nanofilms.^{19,20} Vollath et al. also studied the uphill polymorphic phase transitions in zirconia to develop phases that had previously only been seen as high temperature structures, however they exhibit a reduced density.²¹ The reduced density was seen in a number of compounds explored by Vollath including TiO_2 and HfO_2 .²¹ Chang and Johnson also observed that nanoparticles below 10 nm are intrinsically disordered.²² Since uphill phase transformations have been seen across a variety of materials in literature including the above referenced, it is hypothesized that nanoscale hydroxyapatite below 10 nm will exhibit similar phenomena when successfully synthesized.

Previously published thermodynamic modeling and experimental verification of a room temperature hydroxyapatite synthesis precipitation method revealed that the calcium acetate-potassium orthophosphate system may produce nanoscale hydroxyapatite below 10 nm.²³ X-Ray diffraction (XRD) patterns showed severe peak broadening in the synthesis of non-stoichiometric hydroxyapatite. This precursor system also has advantages of producing hydroxyapatite in a very short reaction time in high yield and uses benign processing conditions, making it the best system to explore for the present hypothesis.

3. Experimental Procedure

The reaction precursors used were calcium acetate hydrate (99%, Acros Organics, Morris Plains, New Jersey) and potassium phosphate tribasic monohydrate (96%, Acros Organics, Morris Plains, New Jersey) and were used as received with no further purification or treatment to make 1.0 m and 0.6 m stock solutions, respectively. The solutions were filtered separately through a 0.2 μ m PES membrane Nalgene filter (Nalgene Labware, Rochester, NY) to ensure absence of nucleation seeds. In a typical synthesis setup, 10 mL each of the calcium and phosphate stock solutions were mixed, phosphate being added to the calcium solution. Upon mixing, a thixotropic gel formed, however viscosity diminished with continual stirring yielding a white slurry after 30 seconds. In some cases, 100 mL of a 0.2 m citric acid (Acros Organics, Morris Plains, New Jersey) wash that had been pH adjusted to 8.9 with ammonium hydroxide (Acros Organics, Morris Plains, New Jersey) was added and allowed to stir overnight for the elimination of amorphous calcium phosphate.²⁴ Previously published data indicated that upon firing, an amount of TCP (tricalcium phosphate) formed suggesting an amorphous component may still be present at the end of the reaction. These citrate-washed powders are labeled with a CW indicating citrate washing was done prior to 2 DI (deionized, Milli-Q biocell with RiOs-S, Millipore Systems, Inc., <18 m Ω , Billerica, MA) water washes, centrifugation and lyophilization. The slurry in both preparations was then immediately centrifuged (3000 rpm, Avanti J-26XP, Beckman Coulter, Fullerton, California), washed with DI water for 1-2 cycles where indicated, shell frozen (Labconoco, Kansas City, Missouri), and lyophilized (Dura-Dry μ P, FTS Systems, Inc., Stone Ridge, New York) from 2 to 7 days (where discussed) to prevent significant

agglomeration. In alternative heated dry preparations following centrifugation, the centrifuged concentrate was dried in a 70°C oven for 2 days. Washing cycles were limited to maintain pH above 7 to prevent a monetite phase change as investigated in previous studies.²³ Powder was stored in an airtight scintillation vial in a desiccator (Drykeeper, Sanplatec Corp, Japan, humidity 30%) until characterized at indicated time points.

Preparation of samples for the in-situ times crystallite development study proceeded as above with minor modifications. The time at 0 sample was centrifuged at 7000 rpm following synthesis and the thick wet clay-like mud was measured directly without drying. The time at 5.5-7.5 h samples were aged in the mother liquor for 5.5 hours prior to centrifugation at 7000 rpm and XRD measurement, where the 6.5 h and 7.5 h spectra were taken of the same 5.5 h sample, just 1 and 2 h later.

When preparing samples for HRTEM imaging multiple techniques were employed. In one case, about 0.25 mL of the as-prepared, unwashed slurry was diluted with 10 mL DI water and aspirated on to a Copper grid (Lacey carbon, 200 mesh or Carbon/Formvar, 200 mesh, SPI, West Chester, Pennsylvania) using a nebulizer. In an alternate preparation, a single drop of the unwashed slurry was diluted with 5 mL of ethanol (99.5% anhydrous, Acros Organics, Morris Plains, NJ) and applied drop wise directly onto a Gold grid (Au plated Cu grid, 200 mesh, SPI, West Chester, Pennsylvania).

Karl Fisher Titration samples were made of the powder through the following process: 0.5 g of the as prepared and aged powders were each ultrasonicated in 14.0 g of anhydrous methanol (99.8%, Aquastar anhydrous methanol, EMD chemicals, Gibbstown,

NJ) for 15 minutes and centrifuged at 6500 rpm for 15 minutes. The liquid was transferred to a filtered syringe and injected into a scintillation vial until analysis. The same filtration procedure was applied to anhydrous methanol as a standard background water measurement.

Characterization of the nanopowders was performed via XRD (Siemens Xrystalloflex, 30 mA, 40 kV, $\text{CuK}\alpha$, 10-80°, 0.03 step, 2-10 s dwell, hydroxyapatite standard pattern, PDF 01-074-0566, Huntington Beach, CA), HRTEM (JEOL 2010, West Chester, PA, Hitachi HF-2000 FEG-TEM, Parlin, NJ), nitrogen surface area adsorption (BET method, Micromeritics Gemini 2375 surface area analyzer, 4 day outgas at 20°C, ~0.4 g used, Norcross, GA), Helium pycnometry (Micromeritics Accupyc 1300, Norcross, GA), thermogravimetric analysis (TGA, 15°C/min to 900°C, 30 min hold at 900°C, Perkin Elmer TGA7 Thermogravimetric analyzer, Waltham, MA), Karl Fisher titration (KFT, controller model 270 and titration module model 275 KF, Denver Instruments, Denver, CO).

4. Results

Multiple drying techniques were employed to thoroughly investigate the optimal method needed to prevent agglomeration and yield the most stable nanopowders. To investigate the fundamental crystallization processes through the synthesis and drying procedures prior to storage, XRD spectra were taken at the initial time point just following centrifugation (no drying) and after 2 days of drying the powder each via freeze drying or oven drying, shown in Figure 1. Although the results show a very broad pattern obscured by the water present and possible nanocrystalline characteristics, the

initial pattern and 2 day freeze-dried patterns share an identical main peak centered around $29.5\text{--}30^\circ$, a slight shift from the hydroxyapatite main peak centered around 31.5° . The shift could indicate a different calcium phosphate structure is initially present, or that the hydroxyapatite structure has incorporated water or severe disorder within the structure, broadening the pattern. The other peak present in the initial pattern centered around 42° , however, does not line up with the broad peak seen around 48° in the 2 day freeze-dried pattern. A possible explanation could be the 2 days under vacuum has created a more stable structure through the bulk, whereas when just synthesized, 2 different structures may have been present and further obscured by excess water. It is noteworthy that the 2 day freeze-dried pattern is identical to the pattern observed after 5 months of storage in Figure 2(a), suggesting this disordered/nanocrystalline phase may be the most stable when producing powders in this size range.

In the alternative heat drying method shown in figure 1 (b), it is evident that the increased temperature drying allowed a significant amount of grain growth and crystal orientation in the c-axis direction (common rod-like morphology) seen by the pronounced peaks at 26° (002) and 53° (004). The pattern remained consistent even after 5 months of desiccated storage, indicating the grain growth produced stable crystals beyond the metastable size range ($<10\text{ nm}$).

XRD results for both as-synthesized and citrate-washed powders after freeze drying for 7 days are shown in figure 2. These initial patterns index closely with hydroxyapatite when synthesized in both regular and citrate-washed conditions. The initial citrate-washed (CW) main powder pattern does show slightly sharper peaks than the as synthesized powder indicating some amount of amorphous phase may still be

present at the end of the reaction after freeze drying 7 days, however, this procedure does allow additional particle maturation and larger grain sizes, which could also explain the narrowing in the peak pattern. Rietveld refinement results from these patterns produced inconsistent crystallite size results (0.8-5 nm) likely stemming from the severe convolution, or combining of the characteristic peaks, seen in the principal hydroxyapatite spectra. Rietveld results were excluded from the data set and particle/crystallite size measurements were pursued via other methods. Furthermore, it has been previously documented that XRD should not be relied on singularly to determine crystallite size of nanoparticles, as other techniques should be used to verify results due to the detection limitations of the technique with this size range.^{25,26,27} The patterns after 5 months of desiccated storage also shown in figure 2 show a drastic reduction in crystalline peak characteristics, possibly suggesting an uphill amorphous phase transition during dry storage may have occurred in both preparations. The main question this poses is whether this is a polymorphic transition or a chemically induced structural change. Since it happened in more than 1 sample preparation method, it may be characteristic of hydroxyapatite in this size range (<10 nm).

During the heat drying method in figure 1 (b), an anisotropic crystal orientation was observed in the c-axis. An in-situ time study was conducted to determine if this was due to the heat treatment, or if this common hydroxyapatite anisotropic growth direction happens during an Ostwald ripening in the mother liquor solution. Figure 3 confirms that even without any accelerated drying methods via heat or vacuum, the crystallite coarsening and orientation is observed as the increasingly pronounced (002) and (004) planes are marked with an asterisk.

To clarify the chemistry and source of structure obscuration seen in figure 2, an in-situ temperature study was performed on the 7 day freeze-dried 5 month storage aged powder and presented in figure 4. It was seen that no structural change occurred until around 500°C, where a dominant hydroxyapatite phase developed with a small component of potassium calcium phosphate (PDF 00-033-1002) impurity from precursor residues. This indicates the chemistry and structure of hydroxyapatite is present, however, the nanocrystallites are too small or contain too many defects to have any long range order. It is also debatable what constitutes long range order, as in most materials 2 nm is not considered long-range. The extremely broad pattern from the aged powder developing into a narrow crystalline hydroxyapatite pattern at these temperatures would be consistent with the assumption that there is a large amount of structural water present in the nanocrystals that is removed through the common practice of heat treatment. It is also interesting, however, that the heat treatment did not yield a structure with c-axis orientation as was seen in the 2 day heat dried sample, indicating a non-rod-like morphology, possibly spherical.

The overall schema for the phase transitions can be mapped as the following: wet synthesized powder (amorphous + nanocrystalline mix) → 2 d freeze-dried powder (amorphous + nanocrystalline mix) → 7 d freeze-dried powder (nanocrystalline on the lower limit of detection, but resolvable peaks) → 5 month storage powder (identical pattern to the 2 d freeze-dried pattern, amorphous + nanocrystalline mix). To further clarify the size classification, high resolution TEM was used to investigate the nanocrystallite size and lattice characteristics of the hydroxyapatite prior to any drying methods.

High resolution TEM was the primary method used to determine size and morphology and is presented in figures 5 and 6. Since sample preparation is crucial in TEM, two different methods were used and both presented. In figure 5, immediately after synthesis, DI water was used as the diluting medium and a nebulizer was used to aspirate the solution onto a copper grid. The imaging outcome still had a very high particle concentration, however the outlines of separate particles were readily seen, assisting in particle size determination. The images confirm an average particle size of the as synthesized powder as under 10 nm, but also show a relatively uniform size distribution. Image analysis of the lower magnification micrograph in figure 5 (a) yields an average size of 2.7 nm, however higher magnification images such as those in Figure 4 (b-c) indicate it should be closer to 5 nm. When measuring the spacing between the lattice fringes on figure 5 (c), a measurement of 0.28 nm is found corresponding to the hydroxyapatite (211) plane. In the literature, the selected diffraction images commonly show both the (002) plane and the (211) plane, suggesting it is not uncommon and has been observed before. Morphologically, the spacing was found to be the same in all the particles, allowing the conclusion of disc-like particles rather than spherical, as spherical would present random spacing measurements in each separate particle.

The alternative TEM sample preparation results presented in figure 6, employed the more traditional route of ethanol dilution of the liquid sample and adding it drop-wise to a gold grid. The initial sample synthesis preparation in figure 6 (a-b) was identical to that presented in figure 4 and confirmed the same size scale and lattice spacing results, however the particle surface boundaries were much harder to delineate than the water preparation. To observe any XRD c-axis growth over solution maturation time, a portion

of the synthesis solution was aged for 5 hours prior to sample preparation. The results show an elongation of the particles into a c-axis developing rod-like morphology (figure 6 (c)), which is consistent with observations commonly found in literature when long synthesis times are employed.

TEM was also done on the 5 month aged powder as a comparison and confirmation of the change observed in XRD (Figure 7). A noticeable particle coarsening was seen and the amorphous-type particles were extremely beam sensitive and began to sinter during focusing. The particle size increase from below 10 nm to almost 40 nm suggests the high surface area nanoparticles were not stable as an individual crystalline form, causing clustering and amorphization to minimize surface area and the incorporation of water to maintain chemical equilibrium with the atmosphere. To further confirm the particle size range at each time point, surface area measurements were pursued via BET method.

Nitrogen adsorption measurements were valuable in determining surface area and a calculated particle size, however, traditional outgassing practices proved problematic in obtaining consistent data across 3 samples, especially for the initial as-synthesized powder. It was expected that high temperature degassing should be avoided to prevent any structural or surface changes, but it took more than 4 days at room temperature to outgas the powder enough to get a repeatable reading across 3 samples ($\pm 10 \text{ m}^2/\text{g}$). Additionally, the powder was so light, 0.4 g was enough to fill the tube which was further complicated by the extra care required in filling the tube as the severe electrostatic charges on the particles caused the powder to more often form a low density aerosol rather than a dense pack to fill the tube.

Surface area measurement results of the powders investigated in figure 2 are presented in Table 1. The corresponding particle sizes were calculated using equation (1), where S_A is specific surface area, ψ_a/ψ_v is shape factor (SF, ratio of morphology area shape factor to volume shape factor), \bar{a} is mean particle size, and ρ is density.²⁸

$$S_A = (\psi_a/\psi_v)/(\bar{a} \cdot \rho) \quad (1)$$

Multiple shape factors (SF) are included to demonstrate the effect of this parameter on the calculated particle size when the morphology is not known. Spherical particles have a shape factor of 6, whereas a platelet may be as low as 4 or as high as 14 depending on dimensions. Equation (2) shows a simplified method of estimating shape factor of a cylindrical shaped platelet-type particle when exact dimensions may not be known. This utility additionally yields morphology information when calculated size is confirmed with the other methods.

$$SF = 2(1+C) \text{ where } C = \text{radius/length} \quad (2)$$

With a particle size in the nanoscale, a slight change in assumed shape factor can vastly affect the calculated size²⁹ as shown in table 1. The density of the powders was measured initially as 2.50 g/m³ and 2.26 g/m³ after 5 months, which is consistent with the reduced density of nanoparticles observed by Vollath et al. as the theoretical density of hydroxyapatite is 3.15 g/m³.²¹ Using the assumed spherical shape factor of 6, the average calculated particle size was around 10 nm before storage, about double what is seen in XRD and TEM, indicating this shape factor may be off. If the shape factor, instead, is

assumed to be 3, the estimated particle size is found to be around 5 nm, which would confirm previous methods. Using equation (2), if the shape factor was 3, the constant C would be 0.5, indicating the cylinder is twice as tall as the radius. Being that it is not likely only the (211) plane would be seen if this were the case, there is also the possibility that during sample preparation the excessive outgassing times needed to consistently measure the powders may have facilitated the beginning of a phase transformation causing particle coarsening. The decrease in surface area by over 300% and decrease in density by 10% along with the corresponding increase in calculated particle size by 370% after 5 month dry storage indicates a significant change has taken place, consistent with XRD results. Possibilities may include surface aggregation due to water adsorption or some phenomena involving particle coarsening in the solid state.

To further investigate the crystalline to amorphous change and determine if it is due to a chemical change involving water or hydroxyls, TGA (figure 8) and a KFT analysis was done on an aged, freeze-dried sample from figure 1 and on an aged, heat-dried sample from an identical preparation as seen in figure 2. TGA revealed a 4% difference in weight loss between the heat dried aged sample and the as prepared aged sample, with the majority of the changes happening around 500°C, where structural water is removed. The as prepared aged powder did not give off the structural water until 50°C higher than the heat treated powder, possibly alluding to an excess of hydroxylation in the powders that produce a nanocrystalline/amorphous pattern after 5 months in storage. KFT also revealed the as prepared aged powder to have 786 ppm more surface water than the heat dried aged powder suggesting it may be a combination of surface water and structural water contributing to the broadening of the pattern seen in figure 2. When the

raw data is normalized, the heat dried aged powder contains 5.13% water (12% weight loss), whereas the as prepared aged powder contains 7.33% water (17% weight loss), which confirms the difference in weight between the two samples seen via TGA (in parentheses). This also reveals that about half of the water contained in the samples is surface water, while the other portion is structural water.

Although the size range objectives of the research were achieved with hydroxyapatite below 10 nm, the characterization of the product was more difficult than expected. The uphill phase transition phenomena seen in other materials also appeared to occur through a crystalline to amorphous phase transition in this nanoscale hydroxyapatite when freeze drying was employed as the drying method.

5. Discussion

The most interesting phenomenon seen in this research is the observed crystalline to amorphous uphill phase change of the nanoparticles over the 5 month period in dry storage. In both sample preparations of water-washed and citrate-washed, the broad XRD patterns of the 5 month powders indicate the reduction of crystallinity in the powder with time sitting at ambient conditions. The topic of discussion is whether this is a chemically induced structural change or a polymorphic change.

A chemical change in this case may cause a structural change due to the high surface reactivity of nanoparticles. The disordering structural change may be facilitated by chemical and structural water incorporation that starts at the surface and propagates inward, causing a change in the overall chemical makeup of each particle (severe hydroxylation) and disrupting crystalline characteristics present. The initial

amorphous/nanocrystalline pattern seen at synthesis and after 2 days of freeze drying is likely to have a significant amount of water within the precipitated structure, being an aqueous reaction medium, making the amorphous/nanocrystalline phase mixture more stable. Over 7 days of freeze drying under vacuum, however, the crystalline structure may become the more stable polymorph, allowing the water to be removed and the powder completely dried in its nanocrystalline form (confirmed by XRD). The Vacuum assisted crystallization was also seen when imaging the particles under the electron microscope, as it took about 15 minutes under high vacuum before significant crystal structure could be seen at high resolution. It is likely that the extremely high surface area of this powder produces such high surface energy, that when bulk powder samples are taken out of vacuum conditions, where water is present, it re-adsorbs the water on to the surface, much like a desiccant. With particles on the nanoscale, especially under 10 nm, the water is bonding to a much higher number of surface sites than in the larger particles. With particle size on the order of 5 nm, it is not outlandish to consider that a structural incorporation of water on the surface may cause a significant disorder within the particles and localized surface amorphization, keeping in mind the surface comprises the majority of these nanoscale particles. Yet, the structural change does not explain the drastic decrease in surface area, but aggregation, coarsening, and disordered hydrogen bonding at particle-particle contacts may. Figure 9 puts forth a schematic of localized ambient water causing a hydrated surface state, prompting hydrogen bonding and disorder, coarsening, and the presence of residual or vacuum induced crystallites in the amorphous aggregate.

It has been seen that phase stability in nanoparticles can be reversed in the solid state due to particle-particle contacts and surface water induced structural transitions.³⁰ For hydroxyapatite, this would be the transition from crystalline to amorphous since other stable phases and structures are dictated widely by pH fluctuations in solution and calcium-phosphate chemical composition. The surface can also be responsible for the growth of nanoparticles in air stemming from electrostatic interactions in orientation and alignment prompting coarsening.²⁹ Although the electrostatic interactions may not be the case, these arguments confirm that chemical changes on the surface can initiate structural changes through particles. However, in the case of this hydroxyapatite it was irreversible because removing the surface water did not reverse the structural change seen throughout until around 500°C, where the particles have had all structural water removed and sintering had started, producing a crystalline pattern once again, but with significantly more narrowed peaks. Although the phase transformation observed can be considered uphill, the agglomeration and minimization of surface area typical of nanoparticles was an expected downhill transformation.

6. Conclusions

The powder synthesized using the calcium acetate-potassium orthophosphate synthesis system produced hydroxyapatite particles under 10 nm, confirmed by multiple characterization methods. The hypothesis that an uphill phase transformation exists in this material as with others of this size range proved true, emphasizing particle characteristics in the nanoscale are drastically different from what is commonly predicted and observed in the bulk. The uphill phase transition was postulated to be both a

structural change and a chemical change, although a surface chemical interaction may be the initiating factor for the inward structural change due to the high surface reactivity of nanoparticles in this size range.

7. Acknowledgements

The authors would like to thank Dr. Peng Li and Dr. Valentin Starovoytov for their help with the electron microscopy, the Rutgers-NSF IGERT DGE 0333196, NASA GSRP NNG04GO44H. A portion of this research conducted at Oak Ridge National Laboratory's Center for Nanophase Materials Sciences was sponsored by the Scientific User Facilities Division, Office of Basic Energy Sciences, U.S. Department of Energy. Research at the ORNL SHaRE User Facility was supported by the Division of Scientific User Facilities, Office of Basic Energy Sciences, Office of Science, U.S. Department of Energy.

8. References

- ¹ VESTAsync™. Online. Available: <http://www.mivtherapeutics.com/>
- ² J C Elliott (1994). Structure and Chemistry of the Apatites and Other Calcium Orthophosphates. Amsterdam, Elsevier.
- ³ J R Woodard, A J Hildore, et al. (2007). "The mechanical properties and osteoconductivity of hydroxyapatite bone scaffolds with multi-scale porosity." *Biomaterials* 28(1): 45-54.
- ⁴ P Pripatnanont, T Nuntanaranont, et al. (2007). "Osteoconductive Effects of 3 Heat-Treated Hydroxyapatites in Rabbit Calvarial Defects." *Journal of Oral and Maxillofacial Surgery* 65(12): 2418-2424.
- ⁵ P Habibovic, T M Sees, et al. (2006). "Osteoinduction by biomaterials - Physicochemical and structural influences." *Journal of Biomedical Materials Research Part A* 77A (4): 747-762.
- ⁶ P V Giannoudis, H Dinopoulos, et al. (2005). "Bone substitutes: An update." *Injury* 36(3), (Supplement 1): S20-S27.
- ⁷ J B Park (1987). Biomaterials Science and Engineering. New York, Plenum Press.

- 8 W Suchanek, M Yoshimura (1998). "Processing and properties of hydroxyapatite-based biomaterials for use as hard tissue replacement implants." *Journal of Materials Research* 13(1): 94-117.
- 9 E Engel, A Michiardi, et al. (2008). "Nanotechnology in regenerative medicine: the materials side." *Trends in Biotechnology* 26(1): 39-47.
- 10 S B Goodman, T Ma, et al. (2006). "Effects of orthopaedic wear particles on osteoprogenitor cells." *Biomaterials* 27: 6096-6101.
- 11 P Habibovic, T M Sees, et al. (2006). "Osteoinduction by biomaterials - Physicochemical and structural influences." *Journal of Biomedical Materials Research Part A* 77A(4): 747-762.
- 12 B Ben-Nissan, A Milev, R Vago (2004). "Morphology of sol-gel derived nano-coated coralline hydroxyapatite." *Biomaterials* 25(20): 4971-4975.
- 13 G Wei, P X Ma (2004). "Structure and properties of nano-hydroxyapatite/polymer composite scaffolds for bone tissue engineering." *Biomaterials* 25: 4749-4757
- 14 J L Xu, K A Khor, Z L Dong, Y W Gu, R Kumar, P Cheang (2004). "Preparation and characterization of nano-sized hydroxyapatite powders produced in a radio frequency (rf) thermal plasma" *Materials Science and Engineering A* 374(1-2): 101-108.
- 15 R Murugan, S Ramakrishna (2005). "Aqueous mediated synthesis of bioresorbable nanocrystalline hydroxyapatite " *Journal of Crystal Growth* 274(1-2): 209-213
- 16 V Jokanovic, D Izvonar, et al. (2006). "Hydrothermal synthesis and nanostructure of carbonated calcium hydroxyapatite." *Journal of Materials Science: Materials in Medicine* 17(6): 539-546.
- 17 M Uota, H Arakawa, et al. (2005). "Synthesis of High Surface Area Hydroxyapatite Nanoparticles by Mixed Surfactant-Mediated Approach." *Langmuir* 21(10): 4724-4728.
- 18 A Chaudhry, S Haque, et al. (2006). "Instant nano-hydroxyapatite: a continuous and rapid hydrothermal synthesis." *Chemical Communications* 21: 2286-2288.
- 19 R Dingreville, J Qu, et al. (2005). "Surface free energy and its effect on the elastic behavior of nano-sized particles, wires and films." *Journal of the Mechanics and Physics of Solids* 53(8): 1827-1854.
- 20 F D Fischer, T Waitz, et al. (2008). "On the role of surface energy and surface stress in phase-transforming nanoparticles." *Progress in Materials Science* 53(3): 481-527.
- 21 D Vollath, F Fischer, et al. (2006). "Phases and phase transformations in nanocrystalline ZrO₂." *Journal of Nanoparticle Research* 8(6): 1003-1016.
- 22 J Chang and E Johnson (2005). "Surface and bulk melting of small metal clusters." *Phil Mag* 85: 3617-3627.
- 23 C Mossaad, M Starr, R Riman (2009) "Thermodynamic modeling and biomimetic evaluation of current hydroxyapatite synthesis approaches and design." To be submitted to *Chemistry of Materials* (Chapter 1)
- 24 C W Chen, W Suchanek, et al. (2007). "The role of ammonium citrate washing on the characteristics of mechanochemical-hydrothermal derived magnesium-containing apatites." *Journal of Materials Science: Materials in Medicine* 18(7): 1413-1421.
- 25 B D Hall, D Zanchet, et al. (2000). "Estimating nanoparticle size from diffraction measurements." *Journal of Applied Crystallography* 33(6): 1335-1341.
- 26 A Guinier (1994). X-ray Diffraction in Crystals, Imperfect Crystals, and Amorphous Bodies. New York: Dover.

- ²⁷ J W Lee and G D Stein (1987). "Structure Change with Size of Argon Clusters Formed in Laval Nozzle Beams" *Journal of Physical Chemistry* 91, 2450-2457.
- ²⁸ J S Reed (1995). Principles of Ceramic Processing. New York, Wiley & Sons, Inc.
- ²⁹ W H Qi, M P Wang et al. (2005) "Shape factor of nonspherical nanoparticles." *Journal of Materials Science* 40, 2737-2739.
- ³⁰ B Gilbert, H Zhang, et al. (2003). "Special phase transformation and crystal growth pathways observed in nanoparticles." *Geochemical Transactions* 4(1): 20.

Figures

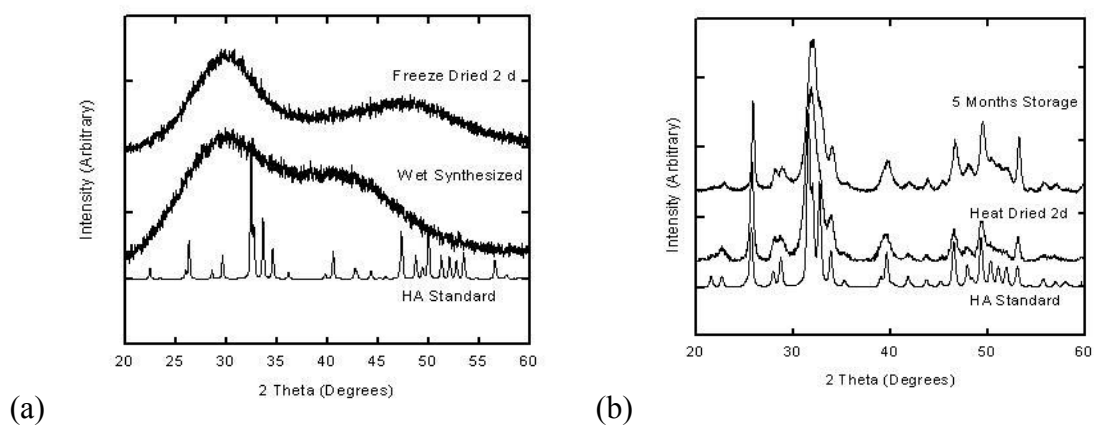


Figure 1. XRD patterns of initial crystal spectra and the effect of short drying methods when (a) freeze drying and (b) oven drying are employed. The initial pattern with no drying is also shown in (a), while the heat dried powder put in dry storage for 5 months is additionally shown in (b)

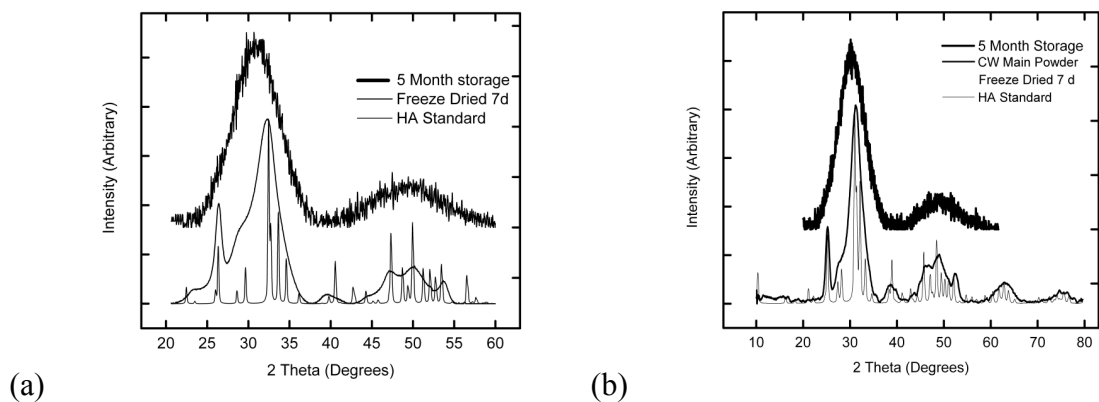


Figure 2. X-Ray Diffraction patterns displaying a severe peak broadening following 5 months at ambient conditions in both (a) DI water washed and (b) citrate washed methods of preparation where initial powder was freeze-dried for 7 days.

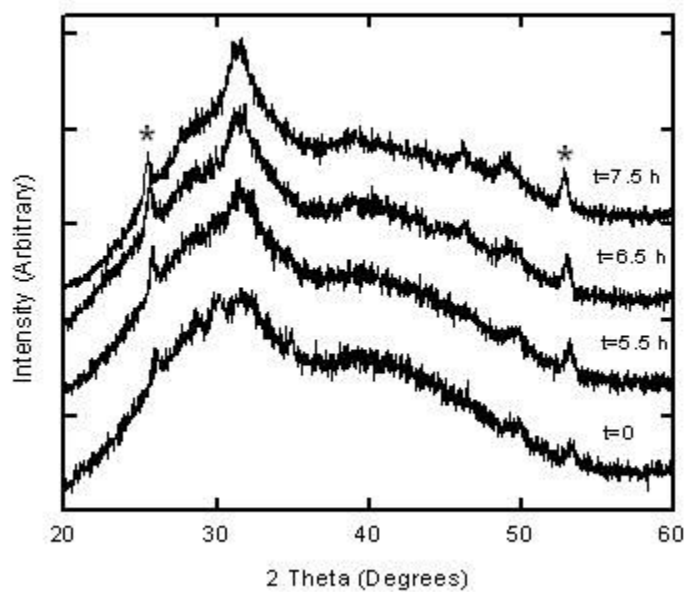


Figure 3. XRD patterns of an in-situ hydroxyapatite crystallite development study taken at 4 time points up to 7.5 hours following synthesis. No accelerated drying methods were employed, showing the c-axis orientation of the (002) and (004) peaks marked with an asterisk.

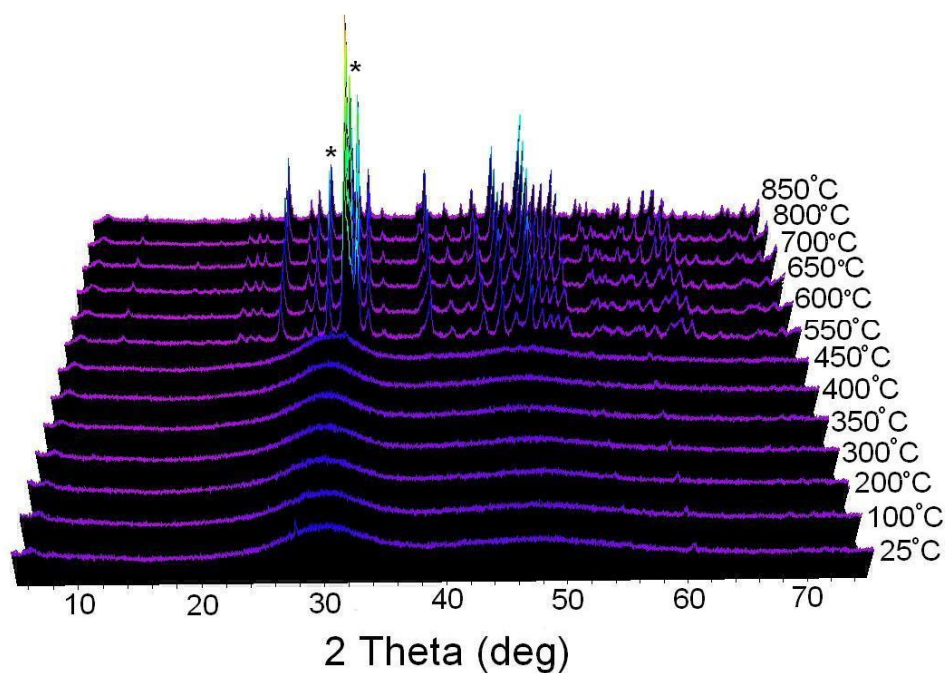


Figure 4. XRD patterns of in-situ temperature study of 7 day freeze-dried 5 month storage powder from figure 4a exhibiting no phase changes until 500°C where structural water is removed and the extreme water obscuration of the crystalline hydroxyapatite peaks is eliminated. Potassium calcium phosphate impurity peaks are denoted with an asterisk (30.1° and 32.4°)

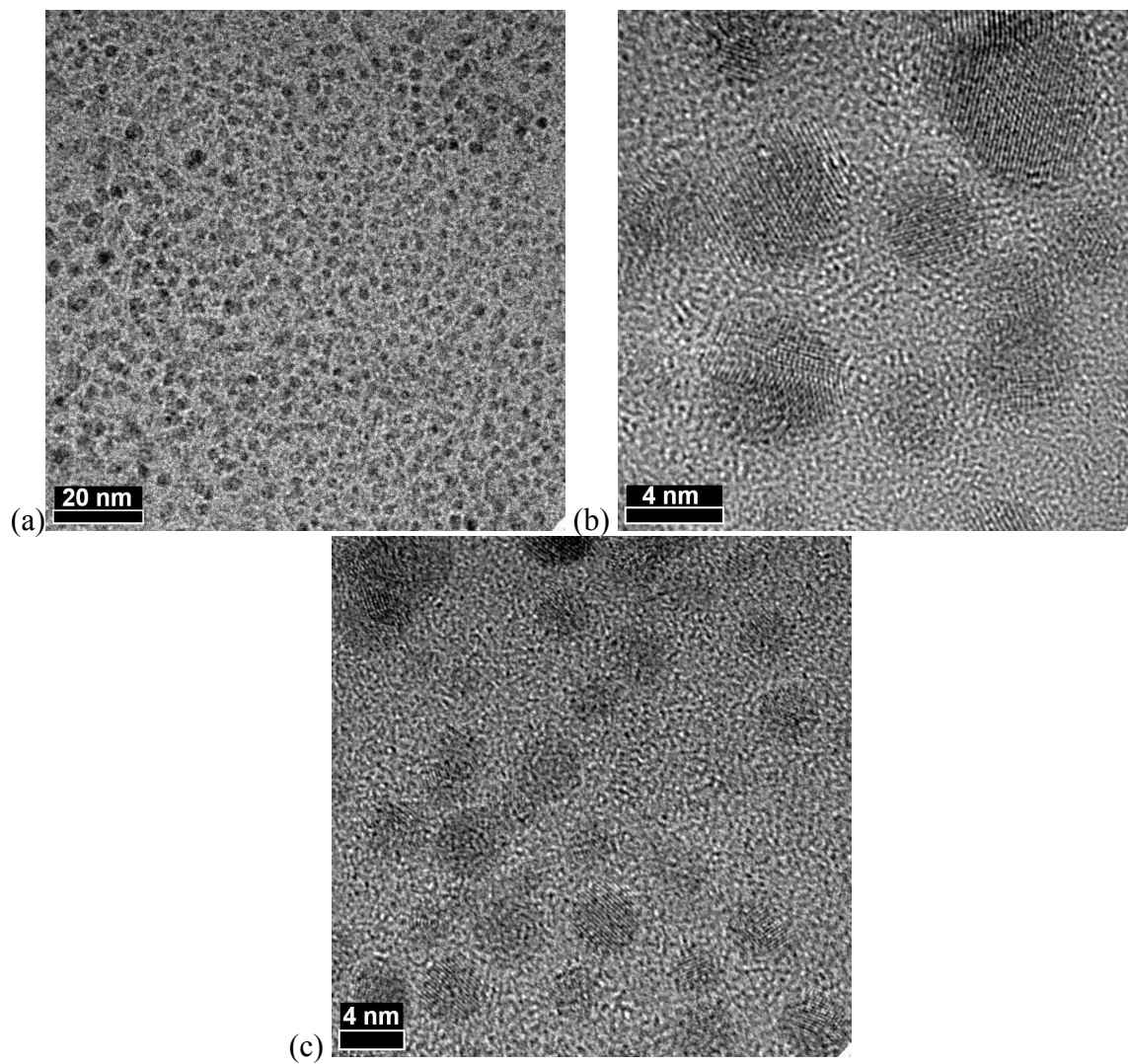


Figure 5. HR-TEM images confirming the size range of the as-synthesized hydroxyapatite to be in the single digit nanometer range and lattice spacings of 0.28 nm. (preparation in mother liquor/water aspirated on Cu-C/Formvar grids)

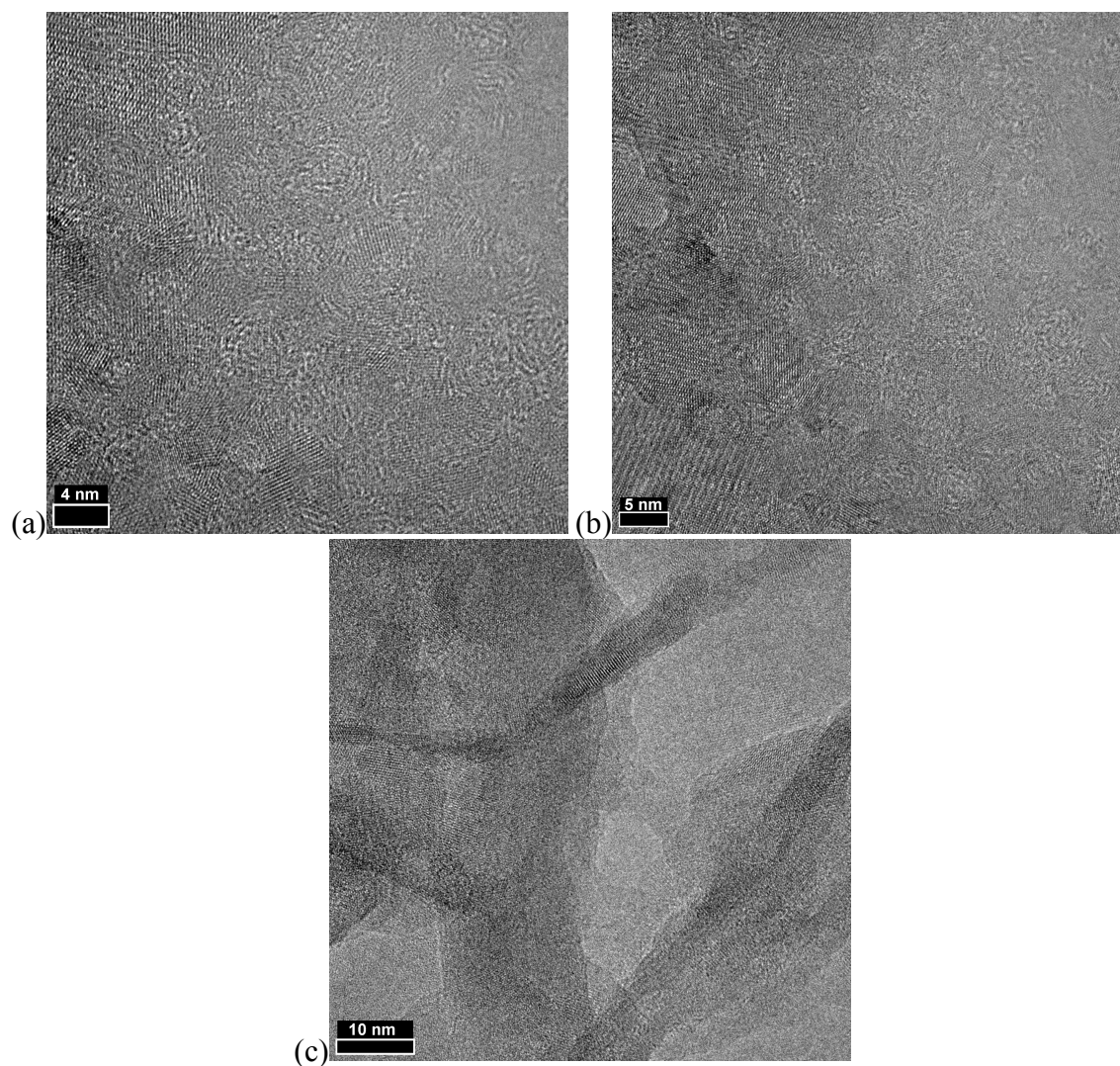


Figure 6. HR-TEM images of ethanol preparation on Au grids showing vacuum induced nanocrystallization and agglomeration. (a-b) as prepared and (c) after 5 hours of aging in solution prior to preparation showing more elongated crystals as c-axis growth is observed. Lattice spacing measurements in (a) reveal the same 0.28 nm spacing of the (211).

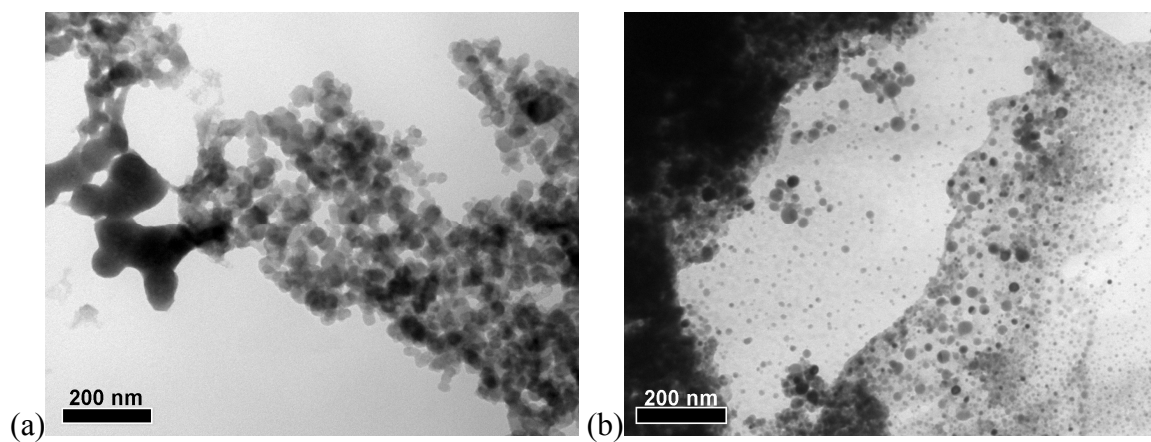


Figure 7. TEM images of the powder after it was kept in dry storage for 5 months.

Table 1. Specific surface area data demonstrating a lowering of surface area and a coarsening of particles over time at ambient conditions.

Sample	Specific SA (m ² /g)	Computed Size (nm) SF=1	Computed Size (nm) SF=2	Computed Size (nm) SF=3	Computed Size (nm) SF=6
CW Main Powder	234.3	1.7	3.4	5.1	10.2
CW Main Powder 1 week	209.2	1.9	3.8	5.7	11.5
CW Main Powder 5 Months	70.1	6.3	12.6	18.9	37.9
Synthesized	259.3	1.5	3.1	4.6	9.3
Synthesized 5 Months	70.9	6.2	12.5	18.7	37.5

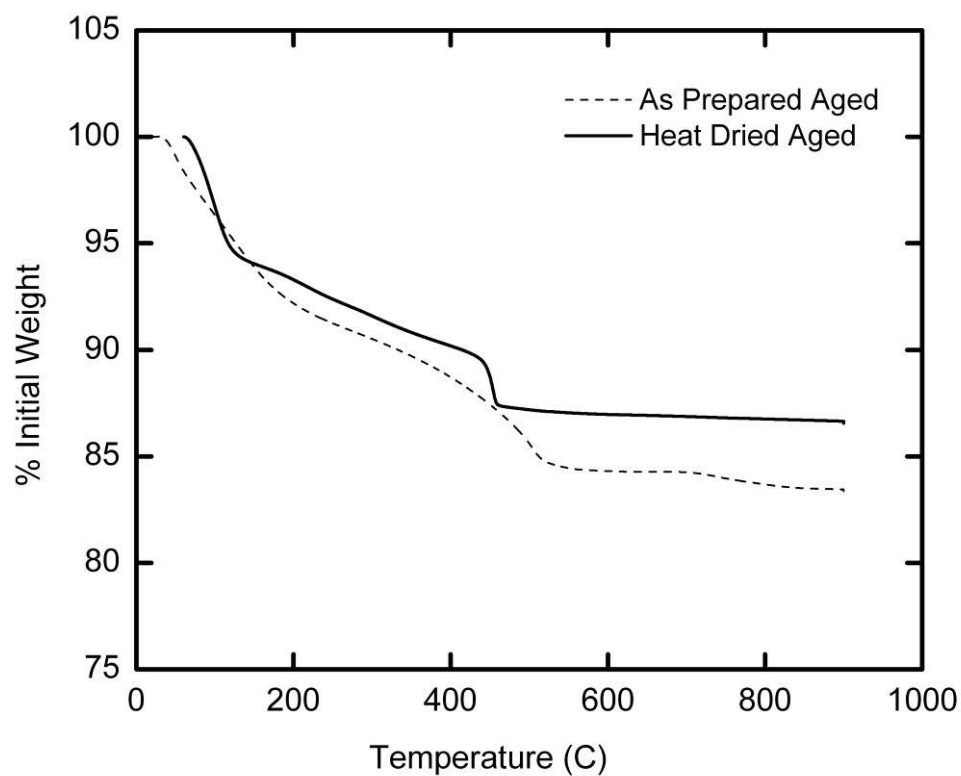


Figure 8. TGA studies comparing weight loss of two drying preparations (heat dried 70°C oven, as prepared freeze-dried) following a 5 month aging period in desiccated storage.

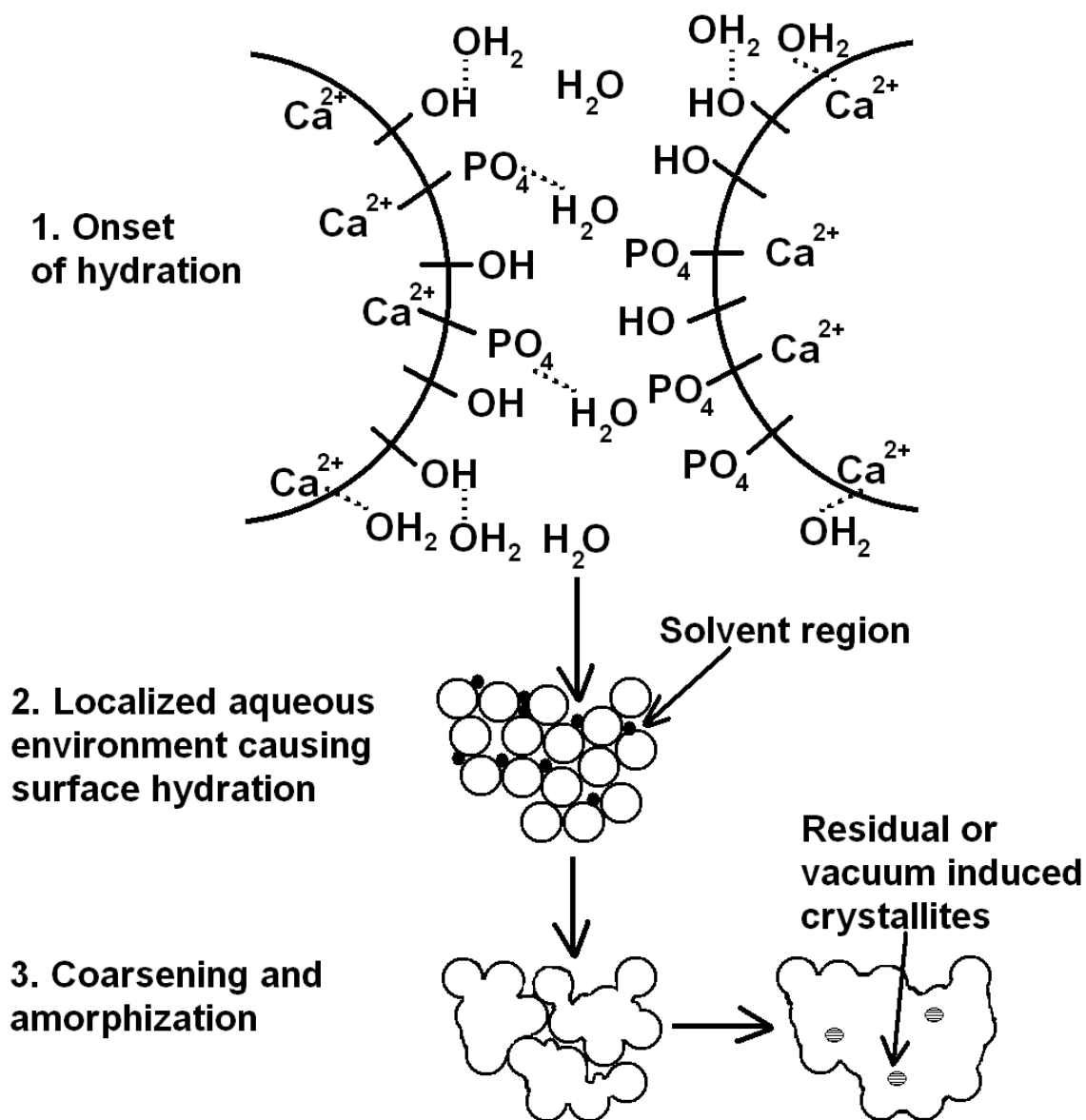


Figure 9. Schematic of molecular water interactions at the surface of the hydroxyapatite nanoparticles, observed to cause uphill crystalline to amorphous structural phase transitions.

Chapter 3

Ectopic Osteoinductive Effects of Demineralized Bone Matrix/Hydroxyapatite Composites on Bone Formation Pathways

Christina Mossaad ^a
Matthew Starr ^a
Anders Petersson ^a
Lawrence A Shimp ^b
Bruce Babiarz ^c
David T Denhardt ^c
Richard E Riman ^a

^aRutgers, The State University of New Jersey, Department of Materials Science and Engineering, 607 Taylor Road, Piscataway, NJ 08854

^bOsteotech, Inc. 51 James Way, Eatontown, NJ 07724

^cRutgers, The State University of New Jersey, Department of Cell Biology and Neuroscience, Nelson Laboratories, Piscataway, NJ 08854

1. Abstract

Hydroxyapatite was synthesized on the surface of allograft collagen fiber forms and tested via ectopic in vivo implantation for observed tissue response effects. Hydroxyapatite was anticipated not only to provide structural support for the allograft, but also to alter the way in which ectopic in vivo tissues respond. Using a previously modeled and explored hydroxyapatite synthesis system that was modified with an inherent buffer, the allografts were aseptically mineralized at 3 different mineral concentrations. These samples and a non-mineralized control were implanted for 28 days in 16 randomized athymic rat models, after which the animals were sacrificed, and the implants were removed and stained to investigate the histology. The 10/6 mM (millimolar, inorganic precursor concentration) mineralized samples produced the same osteoinductivity rating as the control, however the two produced completely different osseous tissue types, suggesting the mineral does significantly change tissue response. Although the osteoinductivity index ratings were same, the mineralized allografts provided a higher mechanical integrity to the implant site, likely allowing a more stable bone turnover surface due to the significant increase in fiber cohesivity afforded by the mineral phase.

2. Introduction

Mineralization by osteoblasts has been observed to occur in the gaps between overlapped collagen molecules, indicating that collagen is the template for this process.¹ This suggests that hydroxyapatite and collagen are components of choice for increased acceptance and performance in biomimetic, osteoinductive implants. While it may not be currently possible to develop pure synthetic hydroxyapatite-collagen complexes for load bearing applications due to poor mechanical properties, it is important to develop fundamental foundations for the technology that will enable it in the future, but simultaneously improve current non-load bearing implant technology through biomimetic technologies.

Type I collagen is the main type found in bone, but over 15 types exist in the human body. Collagen's specific function is to provide tensile stiffness in load bearing, and can provide significant torsional stiffness when mineralized.¹ Collagen currently has many applications in medicine including drug delivery, sutures, aortic wall matrix, corneal shields, wound sponges, wound dressings, skin replacement, and bone scaffolds for spinal and dental applications. As a biomaterial, collagen has multiple advantages and disadvantages—it is plentiful and easily purified, biodegradable, bioresorbable, bioactive, and modifiable, but it is expensive and hydrophobic, which can induce swelling in the host tissue.² A matrix of cross-linked collagen with residual proteins remains when the inorganic component of bone is removed through the process of demineralization.

Demineralized bone matrix (DBM) is widely used as an allograft material in surgeries ranging from dental to spinal, but is limited in load bearing applications due to poor mechanical properties and non-cohesivity of the fibers in aqueous media. Two forms are available—powder and fibers; however, fibers have proven to exhibit superior osteoinduction in application.³ The processing of the DBM is integral in the strength of the scaffold remaining because the acid saturation time and gamma irradiation have proven to alter mechanical properties, emphasizing that any alteration of the material should be biomimetic and mild conditions.^{4,5}

DBM is often coupled with natural and synthetic polymers for cartilage applications, but has not been used widely in load-bearing bone replacement research. This is mainly due to the harsh processing conditions encountered when producing HA, hydroxyapatite ($\text{Ca}_{10}(\text{PO}_4)_6(\text{OH})_2$), the main inorganic component in bone. Traditional HA synthesis methods employ extreme conditions (high temperatures, pHs) and methods (i.e. stirring, reactors) that not only denature the proteins, but also disintegrate the fiber matrix. DBM breaks down in an aqueous environment with a small amount of agitation after minutes, so these traditional hydroxyapatite synthesis methods are not applicable for use with DBM. This downfall allows room for the development of a biomimetic mineralization process that may have a specific application to allograft materials.

The osseous sites of DBM application should lend particularly well to the incorporation of synthetic hydroxyapatite on the surface of the scaffold. Hydroxyapatite has high osteoconductivity^{6,7} and some speculated osteoinductivity⁸, although still under debate. The use of nano-sized hydroxyapatite would further increase the surface area for cell and tissue interaction, likely speeding up the healing and bone formation process.⁹

In the present study, a previously reported room temperature hydroxyapatite synthesis process was altered and used to mineralize DBM scaffolds. The modification employed a slight chemical variation to buffer the synthesis at a neutral pH throughout the reaction on the surface of the fibers.¹⁰ In this study, demineralized bone was dynamically surface mineralized with hydroxyapatite, characterized, and evaluated through an in vivo athymic rat ectopic implantation study. The dynamic precipitation differed from previous non-simulated body fluid precipitation work by utilizing the native calcium sites and precipitating directly onto the collagen. It is hypothesized that the inclusion of hydroxyapatite on the surface of the scaffolds alters the in vivo ectopic tissue response observed.

3. Materials and Methods

GraftonTM DBM (sterile and non-sterile) xenograft plugs from Osteotech, Inc. (Eatontown, NJ) were used as received with no further treatments other than indicated. Two separate sets of reaction precursors were prepared using calcium acetate hydrate (99%, Acros Organics, New Jersey, USA) and potassium phosphate tribasic monohydrate (96%, Acros Organics, New Jersey, USA).

In one set designed for sterile mineralization of the DBM scaffolds, a 100 mM (millimolar) solution of calcium acetate was made and two 60 mM solutions of potassium phosphate were made using DI water (<18 mΩ, Nanopure Ultrapure water system, Barnstead), with one solution neutralized to a pH of 7.6 with acetic acid (99.7% ACS reagent grade, Sigma, St. Louis, MO, USA). This set of solutions was filtered under a sterile hood separately through a 0.2 μm PES membrane Nalgene filter (Rochester, NY)

to ensure sterility and absence of nucleation seeds. These 100 mM calcium acetate, 60 mM potassium phosphate, and 60 mM neutralized potassium phosphate solutions were then divided in half, and additional sets of solutions were made at 10 mM and 1 mM calcium acetate, 6 mM and 0.6 mM potassium phosphate, and 6 mM and 0.6 mM neutralized potassium phosphate concentrations as a variable for study (32 sample implants, 8 control (no mineral), 8 ultralow mineral (1 mM/ 0.6 mM), 8 low mineral (10 mM/6 mM), and 8 moderate mineral (100 mM/60 mM). In the sterile mineralization of each DBM scaffold plug (weight of 124 mg) at each concentration, 10mL of calcium acetate precursor was measured out and placed in each of sixteen 30 mL vials with holes drilled in the screw caps to allow lyophilization (Becton Dickinson, Polypropylene conical tubes, Franklin Lakes, NJ, USA). The DBM scaffold plugs were allowed to soak in the calcium solution at the respective concentrations for 24 hours prior to mineralization. During incubation, the samples were sterilely stored at 4°C refrigerator to suppress contaminant growth. Following incubation, 9.1 mL of phosphate solution and 0.9 mL of neutralized phosphate solution were added and the vials were agitated to elicit crystallization. Plugs were removed and washed with sterile DI water 2 times to agitate loose excess mineral. The pH on the surface of the plug did not fall below a value of 6.5. The samples were then lyophilized within a triple bagged sterile barrier (Cardinal Health, McGraw Park, IL, USA) and maintained until implantation. A 16-animal standard randomization for athymic rat ectopic implant protocol was followed according to standard procedures in place at Osteotech, Inc. The study was conducted for 28-days and samples were explanted, embedded in JB-4 polymer resin, sectioned and stained according to standard histology procedure. Stains used to explore the tissues present

were toluidine blue, hematoxylin and eosin (H&E), and Masson's trichrome to identify both the cellular and extracellular morphology. The scoring system used to rate the 32 nodules was from 0-4, 4 being high osteoinductivity was shown and 0 showing no osteoinductive properties in the ectopic site¹¹. Both the control and 10/6 m concentration scored an average of 3, whereas the higher mineral concentration scored slightly lower at a little above a 2, but all had some samples scored at 3 and 4, showing typical animal variations. The scoring system has up to plus or minus 1 unit in error, indicating the other concentrations may fall in the same statistical category. Chondrocytes were noted to be present in all samples, but were more pronounced in some. The samples that were rated 4 in the control and 10/6 mM concentration were chosen as the comparison in this study to investigate as they yielded the most information about the effect of mineralization on tissue formation.

The other set of reaction precursors designed for materials characterization of the mineralized DBM scaffolds was prepared similarly, but with a concentration of 0.5 M calcium acetate and 0.3 M potassium phosphate solutions. The second set of precursors was filtered under a chemical hood using the Nalgene 0.2 μm PES membrane filters, in a non-sterile manner. Each plug was allowed to incubate at room temperature for 24 hours prior to mineralization and lyophilization as described above.

TEM sample preparation was done by breaking up the fibers in the calcium precursor solution and adding phosphate to initialize precipitation. The low magnification image of the fiber composite was taken with the fiber applied directly to the Copper TEM grid. The higher magnification images were taken after embedding the

fibers in epoxy resin and ultramicrotoming sections. Osmium tetroxide collagen stain was applied where noted.

Solid-state characterization on the non sterile samples was performed via Infrared Spectroscopy (IR, Mattson Galaxy 5000 FTIR Spectrophotometer), X-Ray Diffraction (XRD, Siemens Xrystalloflex, 30 mA, 40 kV, CuK_α), Thermogravimetric Analysis (TGA, Perkin-Elmer TGA 7, 20 °C/min to 900°C), micro-Computer Tomography (micro-CT, Scanco Medical μ -CT 80, machine determined profile settings), and Transmission Electron Microscopy (TEM, JEOL 2010, JEOL JEM -100CX). The solid state characterization was done on samples with a higher concentration of precursors and mineral to be able to qualitatively show the degree of mineralization possible and its chemical and structural impacts, whereas the other concentrations are on the low end of the detection limits, but are more appropriate concentrations for an implantation pilot study.

4. Results

The first results presented are the materials characterization results, which used the higher precursor concentration. The FTIR spectrum shown in figure 1a demonstrates the presence of hydroxyapatite through the increase in relative intensity in the phosphate band around 1020 cm^{-1} . The peaks at 1407 cm^{-1} and 1563 cm^{-1} are from residual acetate ions present following mineralization. Deionized water washing of the composite beyond removing excess particles from the surface was not performed in order to maintain pH above 7. The amide I band of collagen is present in both samples around 1650 cm^{-1} indicating a coating of calcium phosphate is present on the collagen. To verify

hydroxyapatite as the phase produced, XRD was performed on residual powder synthesized from the same reaction and was found to be hydroxyapatite with significantly broadened peaks indicating a nanoscale crystallite size (figure 1b).

Transmission electron microscopy shown in figure 2 (a) reveals a significant deposition of mineral on the surface of formed fibers from the higher 0.5/0.3 M Ca/P concentration of precursors. The micrographs in figure 2 (b) and (c) additionally suggest that some mineral (< 20 nm) may be precipitating within the collagen structure and between the fibers, not just adhering to the surface with weak bonding. Micrographs (b) and (c) were cross sectional images obtained from an embedded sample to show the diameter of the fiber and the mineral precipitated within. Precipitated mineral concentration was denser toward the surface of the fiber and showed a significant amount of clustering. To evaluate the amount of hydroxyapatite present within the non-sterile mineralized composites, TGA was performed on a control DBM sample and a mineralized sample. It was found that the control retained 0.6% of its weight, whereas the mineralized sample retained 7.2%, indicating there was significant mineral deposition within the collagen matrix even following the 2 cycle washing agitation employed in the experimental procedure to wash out excess particles precipitated in solution.

To visually demonstrate the fiber cohesivity improvement, a cube of the control DBM and a cube of the mineralized DBM sample were dropped into separate vials of DI water and agitated vigorously. Figure 3 shows both samples following the agitation, where the control DBM has completely fallen apart and the mineralized DBM has retained its shape, although the collagen has become hydrated with water and caused the composite to swell slightly. While the quantitative mechanical properties of the

composite materials contribute to this research, the in-depth mechanical analysis will be explored in the future to allow due diligence to the current discussion of the biological results from the in vivo testing.

The higher concentration precursors produced a significant amount of excess hydroxyapatite in solution, making it imperative for thorough washing for implantation samples. To avoid these extra steps and subsequent additional chances of breaking the aseptic barrier as well as dropping the pH lower than 6.5, lower limit of hydroxyapatite stability, the concentration of precursors was lowered to 100/60, 10/6, and 1/0.6 mM. These concentrations produce very little excess mineral in the surrounding fluid, ensuring any mineral deposited is on the DBM. A μ -CT image (Figure 4) was taken to verify the presence of mineral within the lower concentration structure (10/6 mM). A DBM control sample with no mineral content would not show any contrast, whereas even at this low inorganic mineral concentration, significant white contrast is seen indicating qualitatively that there is mineral present in the composite. To complement the materials characterization of the composite, the histological characterization revealed a different type of data.

During the explantation of the nodules, it was evident that the mineralized samples had a higher degree of vascularization (pink/red appearance versus gray) and macroscopically felt harder when probed. However, when the samples were sectioned and stained with the traditional toluidine blue, the 10/6 mM concentration scored the same osteoinductivity index (OI) as the control, indicating that activity-wise there was not much improvement when observed with this stain. It is interesting that the highest concentration of mineral did not yield the greatest osteoinductivity, but it is possible that

too high a concentration of synthetic mineral may have masked some of the osteoinductive proteins of interest, lowering the overall score. Figures 5 a, b and 5 c, d show the similarities at 20x magnification of the top scoring samples (10/6 and control, respectively) stained in toluidine blue and H&E. Chondrocytes (dark blue, light purple) are visible in both samples, but appear in higher quantity in the control than the mineralized sample. Osseous tissue appears at high levels in both samples as well as osteoblasts, stained with toluidine blue. In the mineralized sample stained with H&E in 5b, adipocytes and adipose tissue are present throughout, indicating the development of young bone marrow tissue; however, this is only present around the edges of the control DBM in 5d, as chondrocytes dominate a large portion of the nodule. Figure 6 shows a higher magnification view (100x) of the mineralized sample from figure 5 (b) with lines of osteoblasts along the surface of the DBM/HA fibers circled and marked adipocyte (A). The control DBM sample from 5 (d) at a higher magnification shows similar areas only at the edges of the nodule, indicating the surface of the implant is vascularized, but the core may have much less blood flow. Vascularization capacity of an implant is crucial in its bioactivity because the availability of transport into and out of the device is necessary. Specifically with bone, vascularization stimulates bone cell migration to the site for remodeling and plays a critical role in the development of mature bone¹².

To verify the difference between the 10/6 mM and the DBM control sample, additional sections were stained with Masson's trichrome, where the DBM, adipocytes and adipose tissue stain red, and chondrocytes and cartilage stain blue. Figure 7 shows the micrographs at 20x of each sample with this stain. In the 10/6 mM composite, the majority of the nodule is osseous tissue and young bone marrow with a few chondrocytes

and some cartilage tissue, whereas the control DBM shows the majority of the nodule as chondrocyte-rich, with areas of osseous tissue around the edges. It is clear in this stain that vascularization was present on the surface and outer portions of the DBM implant, leaving the center to have significantly less blood flow. This induced the formation of chondrocytes, rather than osteoblasts, directly from the mesenchymal stem cells recruited to the site. When viewed under higher magnification and compared to H&E in figure 8, a difference can be clearly seen. Figure 8c shows the control near the outer edge of the nodule at the interface of the chondrocyte cluster (top left) and the osseous tissue (center). The dense blue chondrocyte cluster seen in the center of the control nodule under trichrome in figure 8 (c) stains a blue/purple in H&E 8 (d), showing a stark contrast to the composite shown in 8 (a-b) containing largely osteoblasts and adipocytes (labeled A, AT (adipose tissue)). The difference in the main tissue types of both samples is demonstrated at high magnification (200x) in figure 9. The majority of the control tissue under high magnification appears as dense chondrocyte clusters as shown which may develop into cartilage-type tissue, whereas the 10/6 mM mineralized DBM contains a few chondrocytes (seen at lower magnification), but mostly adipose-type tissue, which commonly develops into bone marrow-type tissue. The absence of porous adipose tissue in the bulk of the control nodule suggests that the control had much less vascularization and possibly a delay in developing new bone directly from the implant, necessitating an intermediate chondrocyte-induced cartilage stage.

5. Discussion

The two most interesting points of discussion are the possibility of precipitating the hydroxyapatite particles within the collagen structure and the exploration of the main differences in tissue types developed between the composite and control samples.

In regards to hydroxyapatite precipitating within the collagen, it is postulated that the demineralization process leaves sites within the structure of the collagen that have a significant calcium affinity or perhaps reflecting the presence of calcium binding proteins. The initial soak in the calcium precursor allows the complete bonding of calcium ions to these sites, so when phosphate is added, mineralization is occurring within the structure, not just at the surface. If it were simply weak particle-collagen bonding at the surface, the majority of the particles would be released upon washing and lyophilization, likely prompting an immune response, which was not observed.

It may also be the case that within a three dimensional structure of fibers, the mineral serves as a binding agent in the fiber overlaps, increasing both wet and dry state strength. This hypothesis was validated by agitating both a control and a mineralized sample in water; the control completely broke apart and the composite remained intact, just hydrated with an increase in apparent volume. This is also a key point for applications of DBM, as it is generally hydrated prior to implantation and the increased cohesion of the fibers when mineralized facilitates its application to the surgical site with limited fiber debris. The cohesivity of the fibers may also contribute to the types of tissues seen to develop in the composite sample. Seeing two different tissue types develop in the composite and control samples may be due to both chemical and mechanical benefits afforded by the addition of hydroxyapatite.

In the chemical aspect, hydroxyapatite may be facilitating an increase in vascularization. Both osteoblasts and chondrocytes are differentiated forms of mesenchymal stem cells, but the tissue present determines the type—well vascularized areas such as bony sites elicit differentiation of osteoblasts, whereas less and non-vascularized areas such as cartilage elicit differentiation into chondrocytes.

Endochondral ossification is the pathway of embryonic bone formation and postnatal bone growth, eventually giving rise to long bone formation.¹³ Through endochondral ossification, the extracellular matrix cartilage formed by the chondrocytes prior to entering hypertrophy becomes mineralized into bone. The presence of chondrocytes in the control nodule may signal a delay in the formation of bone because this intermediate cartilage was formed. In contrast, the development of adipose tissue and bone marrow in the composite may indicate that these samples were further along in the bone formation process.¹⁴ Bone marrow is the main producer of blood cells and mesenchymal stem cells and commonly used to stimulate new bone formation through the differentiation of mesenchymal stem cell types. It seems in the case of the control, the lack of vascularization prompts the formation of chondrocytes for eventual long bone formation, whereas the mineralized composite elicited the formation of bone marrow and spongy bone. Overall, in this ectopic study, the H&E stain makes the difference between the two samples more apparent, but to untrained eye, they still look very similar, making the trichrome stain a necessity. It is still unclear why the composite elicited a completely different response or which pathway is the superior response. It should not be discounted that in a bony site, the two may be identical, but it would be expected from the literature

that the hydroxyapatite-containing DBM would have a much higher bone growth rate in a bony site.

In the mechanical aspect of the experimental differences, the increased fiber cohesivity and strength may have additionally contributed to the bone marrow tissue-type formation. Biomaterials should have a targeted degradation consistent with the pace of bone growth to allow optimal turnover rates and use of growth factors.^{10,15} When an implant degrades too quickly, the transient surface lacks stability for long term cell attachment, likely developing a very fibrous encapsulation or cartilaginous area devoid of osseous tissue or bone formation. On the contrary, if it takes too long, bone may fail to form due to the recognition of the implant as a foreign body and failure of bone to form at the desired site.¹⁶ In future studies, it would be beneficial to test the optimal mineral level over a longer implantation time to observe the long term biological implications of having hydroxyapatite functionalized demineralized bone as well as comparing the long-term outcome of each type of bone developed with the control and the composite.

6. Conclusions

Hydroxyapatite was successfully synthesized within a demineralized bone matrix and implanted for 28 days in an athymic rat model. The process used a dynamic precipitation of the mineral on the surface of the collagen throughout the DBM, which improved osteoconductive and osteoinductive properties as well as provided extra mechanical support to prevent rapid dissociation. The fiber cohesivity afforded by the mineralization as well as the presence of an osteoconductive inorganic component showed a vastly different tissue-type development over the control despite the same OI

scoring. The HA/DBM composite supported the development of adipocyte-rich bone marrow type-tissue, whereas the control supported the growth of chondrocyte-rich cartilaginous tissue, shown through the staining of the nodules with toluidine blue, H&E, and Masson's trichrome.

7. Acknowledgements

The authors would like to thank Rutgers-NSF IGERT DGE 0333196 and Osteotech Inc. for their generous funding of the research. Special thanks to Ricki Simoskevitz for her sectioning and staining of the histology slides and Dr. Peng Li and Valentin Starovoytov for the TEM micrographs.

8. References

- ¹ Gelse, K, E Poschl, T Aigner (2003). "Collagens—structure, function, and biosynthesis." *Advanced Drug Delivery Reviews* 55: 1531– 1546
- ² Lee, C H, A. Singla, et al. (2001). "Biomedical applications of collagen." *International Journal of Pharmaceutics* 221(1-2): 1-22.
- ³ Martin, G. J., S. D. Boden, L. Titus, and N. L. Scarborough.(1999) “New Formulations of Demineralized Bone Matrix as a More Effective Graft Alternative in Experimental Posterolateral Lumbar Spine Arthrodesis.” *Spine* 24:637
- ⁴ Han, B., Z. Yang, et al. (2005). "Effects of moisture and temperature on the osteoinductivity of demineralized bone matrix." *Journal of Orthopaedic Research* 23(4): 855-861.
- ⁵ Summitt, M. and K. Reisinger (2003). "Characterization of the mechanical properties of demineralized bone." *Journal of Biomedical Materials Research Part A* 67A(3): 742-750.
- ⁶ Giannoudis, P. V., H. Dinopoulos, et al. (2005). "Bone substitutes: An update." *Injury* 36(3, Supplement 1): S20-S27.
- ⁷ Woodard, J. R., A. J. Hilldore, et al. (2007). "The mechanical properties and osteoconductivity of hydroxyapatite bone scaffolds with multi-scale porosity." *Biomaterials* 28(1): 45-54.
- ⁸ Tsiridis, E., A. Bhalla, et al. (2006). "Enhancing the osteoinductive properties of hydroxyapatite by the addition of human mesenchymal stem cells, and recombinant human osteogenic protein-1 (BMP-7) in vitro." *Injury* 37(3, Supplement 1): S25-S32.
- ⁹ Engel, E., A. Michiardi, et al. (2008). "Nanotechnology in regenerative medicine: the materials side." *Trends in Biotechnology* 26(1): 39-47.
- ¹⁰ Mossaad, C., M. Starr, R. Riman. (2009) “Thermodynamic Modeling and Biomimetic Evaluation of Current Hydroxyapatite Synthesis Approaches and Design” In preparation. (Chapter 1)
- ¹¹ Edwards, J., M. Diegmann, et al. (1998). "Osteoinduction of Human Demineralized Bone: Characterization in an Animal Model." *Clin. Orthop. Rel. Res* 357: 219-228.
- ¹² Barou, O., S. Mekraldi, et al. (2002). "Relationships between trabecular bone remodeling and bone vascularization: a quantitative study." *Bone* 30(4): 604-612.
- ¹³ Mackie, E. J., Y. A. Ahmed, et al. (2008). "Endochondral ossification: How cartilage is converted into bone in the developing skeleton." *The International Journal of Biochemistry & Cell Biology* 40(1): 46-62.
- ¹⁴ Wheeler, P. R., H. G. Burkitt, et al. (2nd Edition). Functional Histology :A Text and Colour Atlas, Churchill Livingstone.
- ¹⁵ Lee, S.-H. and H. Shin (2007). "Matrices and scaffolds for delivery of bioactive molecules in bone and cartilage tissue engineering." *Advanced Drug Delivery Reviews* 59(4-5): 339-359.
- ¹⁶ Walton, M. and N. J. Cotton (2007). "Long-term in vivo Degradation of Poly-L-lactide (PLLA) in Bone." *Journal of Biomaterials Applications* 21: 395-411.

Figures

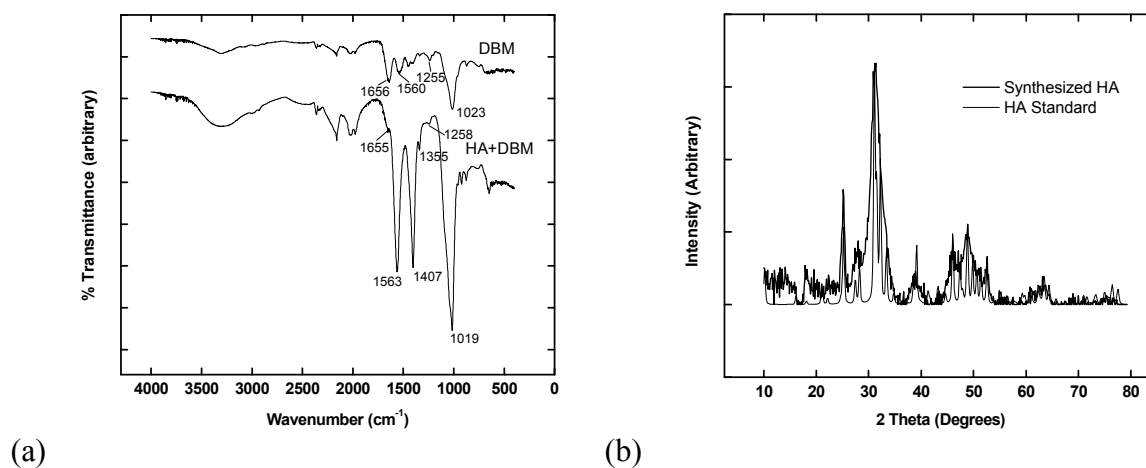


Figure 1. (a) FTIR spectra of the DBM before and after mineralization (0.5/0.3 M) showing a significant increase in the phosphate band around 1020 cm^{-1} and (b) XRD pattern showing hydroxyapatite is the only detectable phase synthesized.

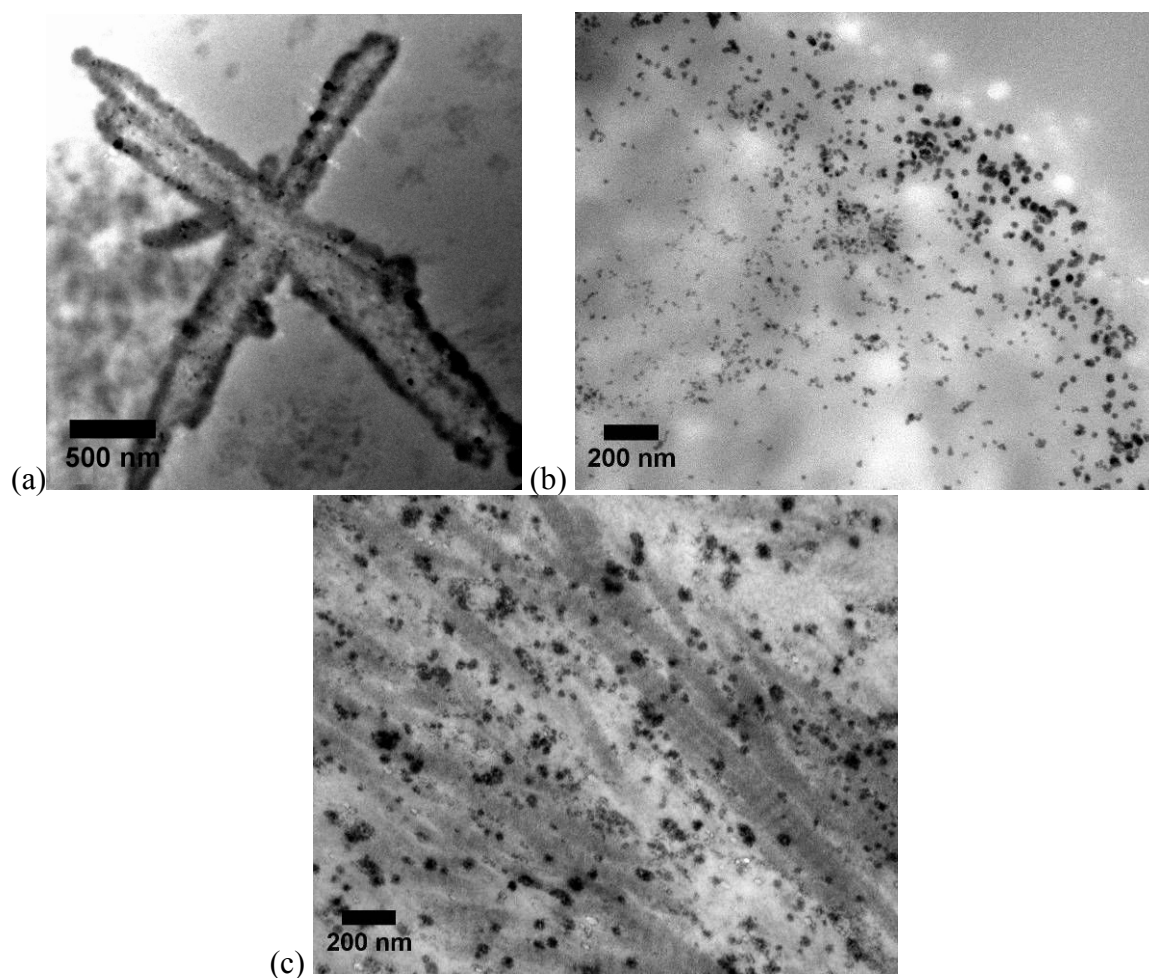


Figure 2. TEM images of (a) mineralized fibers showing successful hydroxyapatite deposition within the surface of the fiber on the macroscopic level where the fibers were placed on the surface of the grid, (b) hydroxyapatite on the surface of the unstained collagen composite cross section and (c) hydroxyapatite on the surface of an Osmium tetroxide stained collagen composite cross section.



Figure 3. Control (left) and mineralized DBM (right) in DI water following intense agitation, demonstrating increased fiber cohesivity afforded by the mineral phase.

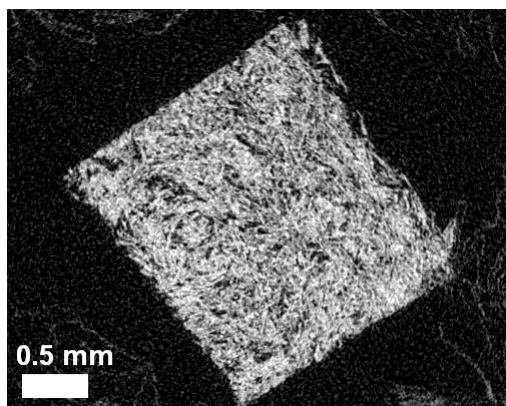


Figure 4. Micro-CT of (10/6 mM) the mineralized DBM at low concentration showing significant and uniform mineral deposition is present by the white contrast of the composite.

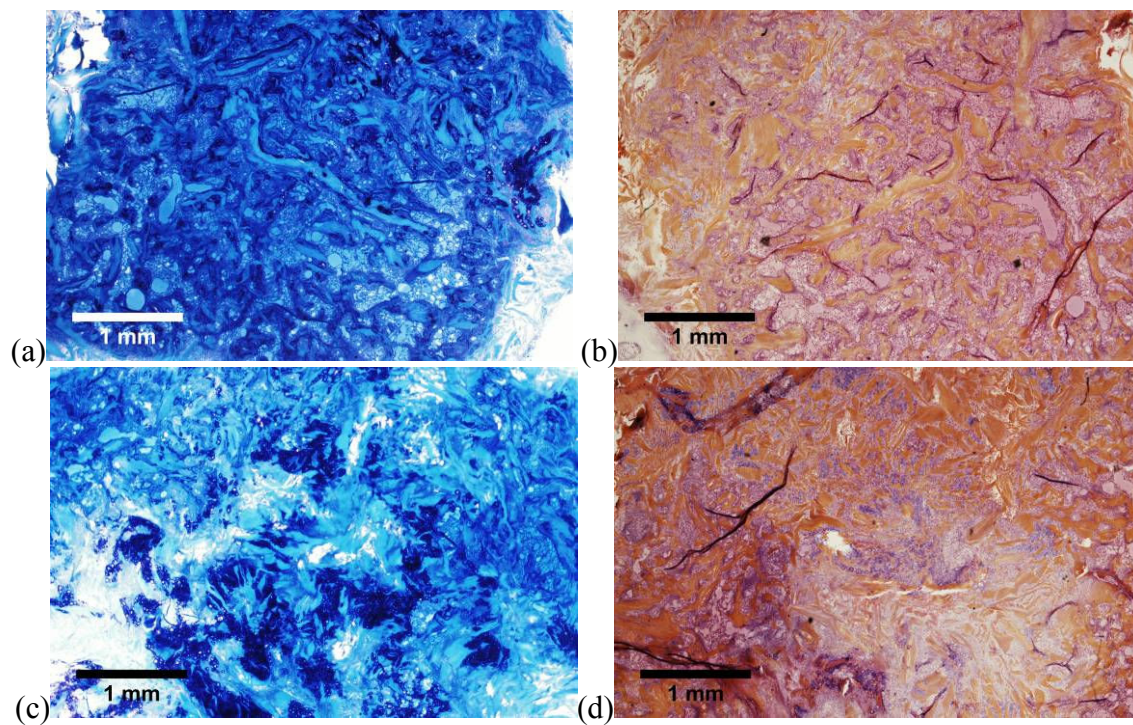


Figure 5. Histological slides in Toluidine Blue and H&E of 10/6 mM (a-b) and the control (c-d). The DBM and HA/DBM in the stains are Light blue and orange/red in Toluidine blue and H&E, respectively (bar=1 millimeter, 20x).

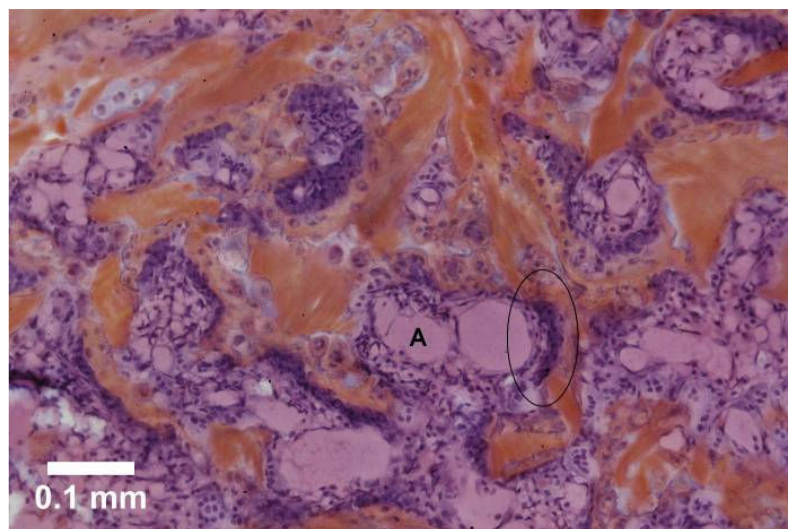


Figure 6. H&E stained section of 10/6 mM mineralized nodule showing presence of (A) adipocytes, and lines of osteoblasts (circled) on the HA/DBM fiber surface. (100x)

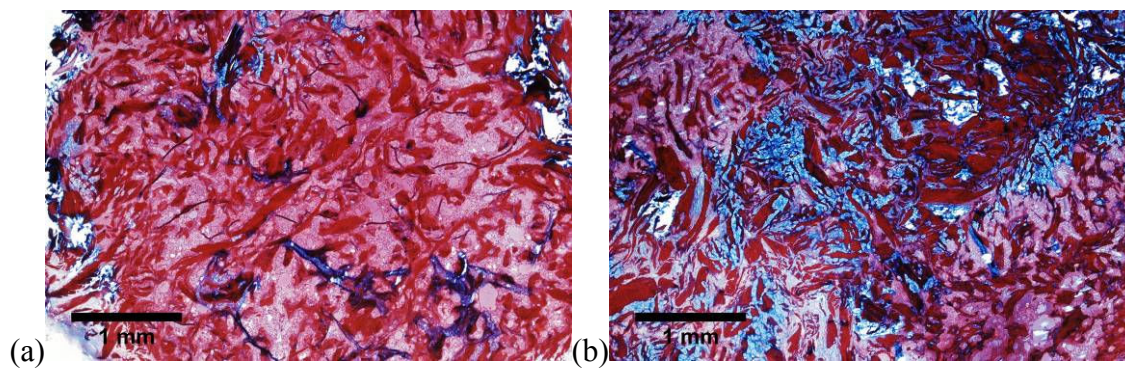


Figure 7. Histological slides of (a) 10/6 mM and (b) control in Masson's trichrome stain showing adipose tissue in red and chondrocytes in blue (bar=1 millimeter, 20x).

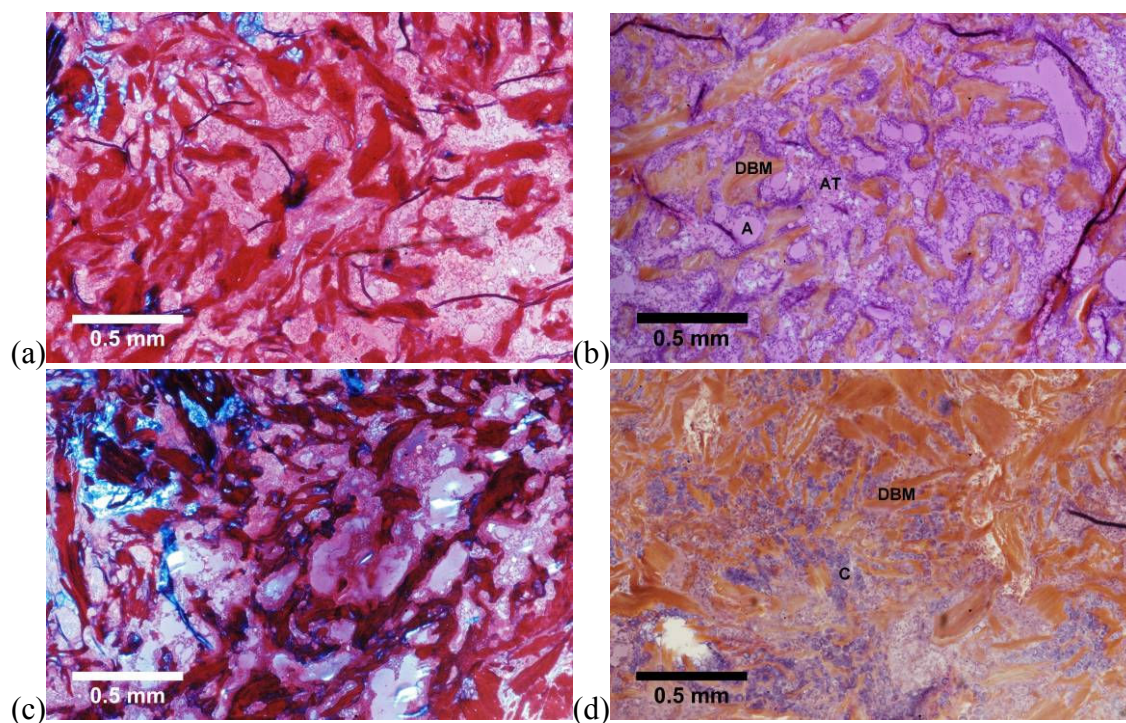


Figure 8. Higher magnification images (40x) of histological slides of 10/6 mM (a-b) and the control (c-d) in trichrome and H&E to show detail of the difference in adipocytes (A), adipose tissue (AT), and degree of presence of chondrocytes (C) in the DBM (orange/red) (bar=0.5 millimeter).

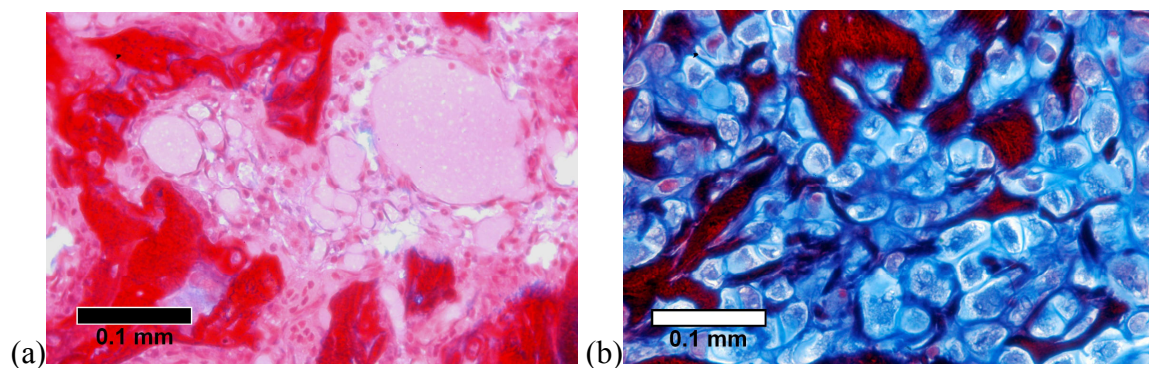


Figure 9. Higher magnification images (200x) of the (a) mineralized 10/6 mM and (b) control histological slides showing two different tissue types that formed at the 28-day time point investigated. (bar=0.1 millimeter)

Future Work

An interesting powder synthesis study to conduct in the future could comprise the crystallite growth kinetics of the particles, mapping the stages they go through from amorphous/nanoparticles (prior to drying or aging) and how they develop in solution over time. The study would also benefit the understanding of how time affects all the parameters studied in the second chapter of this thesis including washing parameters.

The particles could be citrate washed and returned to a calcium and phosphate rich mother liquor and observed if they age at the same rate as without the citrate washing.

The citrate washing, eliminating the amorphous phase should show a very highly developed crystalline structure that remains crystalline after it has grown larger than 10 nm. This study would also aid in future animal model studies where different crystal sizes of different crystallinities are implanted ectopically to observe the changes in tissue response. It is hypothesized that the more crystalline, larger particles will have a lower osteoconductive and osteoinductive capacity than its nanostructured amorphous counterpart presented here. Tissues have been shown to respond more negatively to higher crystallinity calcium phosphate structures initiating encapsulation and immune responses, or just a plain lack of growth as the highly crystalline particles and structures are unable to be resorbed or remodeled by the host tissue. The development of a thermodynamic model involving simulated body fluid would also be of interest as calcium, magnesium, carbonate, potassium, sodium, iron, and other minerals have a significant impact on how mineral is formed as well as tissue responses to the said particles. The same technology reported here could be doped with rare earths for

imaging as well as doped with the previously mentioned minerals to observe any tissue effects. This technology used as radio-opaque imaging is also an interesting application to investigate, as bone degradation or formation over time may be more readily observed as the implantable device is resorbed. This could be accomplished with the development of a composite, an injectable cement or injectable dye using the particles or the aqueous precursor technology. Lastly, the technology could also take an interesting turn if used for drug delivery intravenously or, with such high surface area, as an implantable drug delivery device.

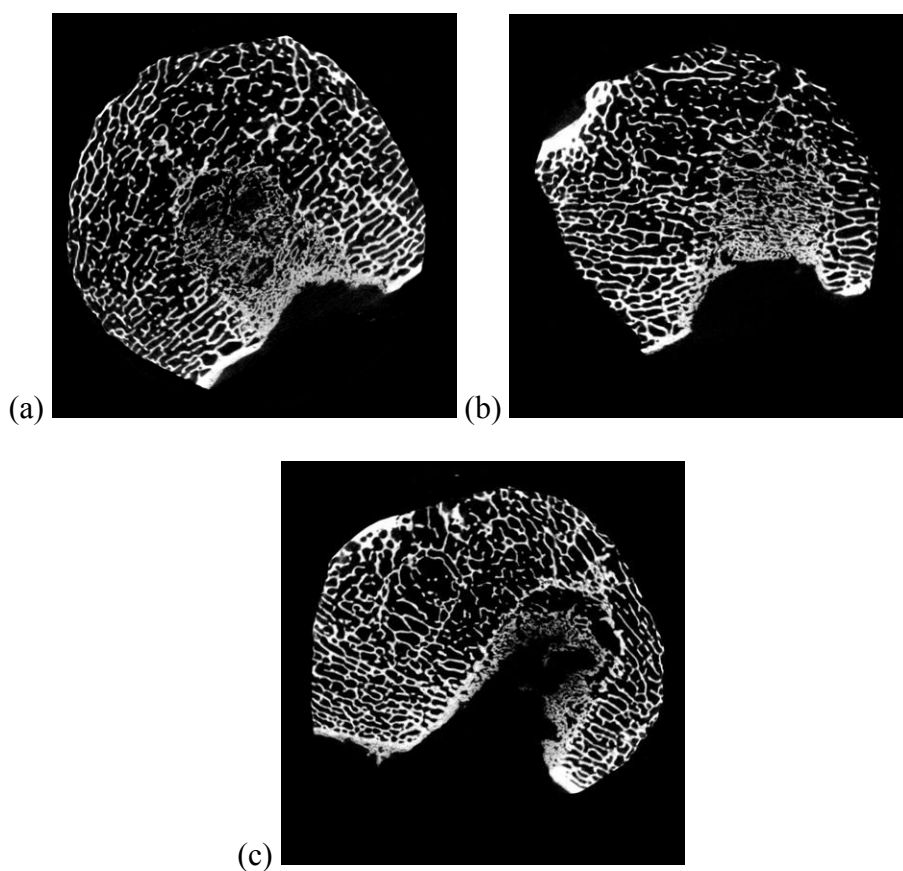
Some important factors to consider with this technology is that glycerol content of the as-received DBM material affects the mineralization levels and hydration time. All residual demineralization acid should also be properly washed out as to not skew the reaction pH. The DBM can also be made with different fiber sizes, which vastly affect mechanical integrity and fiber cohesion following mineralization.

Conclusion

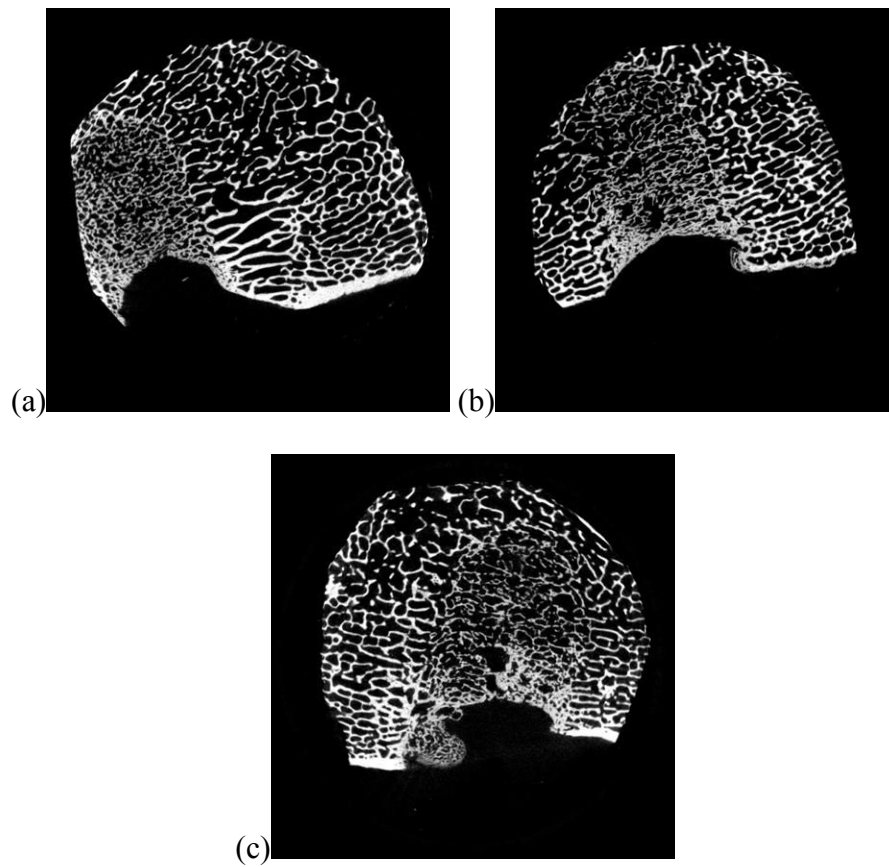
Hydroxyapatite was successfully synthesized at room temperature and neutral pH in fulfillment of the initial goal. The technology was also successfully applied to allograft materials in an aseptic adaptation of the process and evaluated in-vivo against traditional demineralized bone allograft materials. Although the osteoinductivity rating was equal to the control, the tissue response elicited was different, indicating the nanoscale hydroxyapatite exhibited an alternate response on the cellular level. A qualitative structural improvement and fiber cohesivity afforded by the inorganic mineral phase may also have contributed to the alternative tissue response by providing more stable structure for tissue and bone formation in the ectopic site.

Appendix

The following 2 figures are additional in-vivo studies performed in a 12 week bony-site sheep array conducted by Osteotech, Inc. using two different GraftonTM products (putty and matrix) that were mineralized via the same aseptic process. All but one result were reported positive and research will be continued by the company.

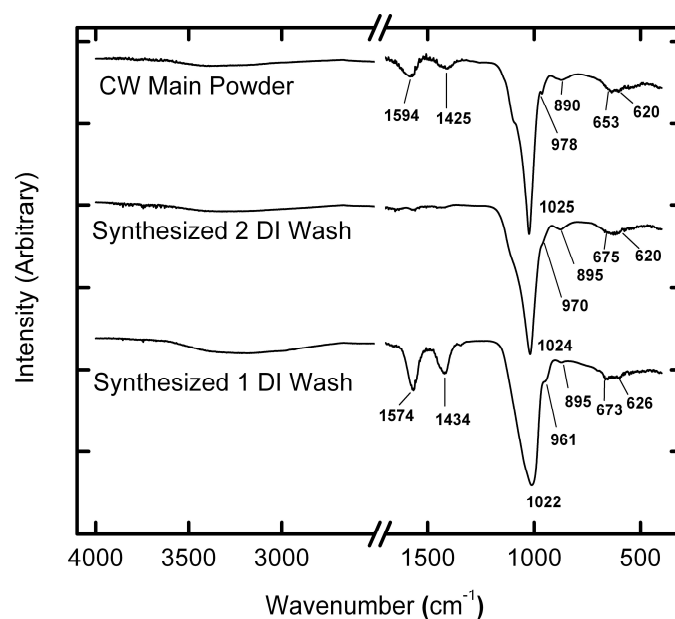


AP Figure 1. (a-c) micro-CT images of hydroxyapatite mineralized allografts on GraftonTM matrix. (c) was the only negative result reported



AP Figure 2. (a-c) micro-CT images of hydroxyapatite mineralized allografts on Grafton™ putty.

IR Spectroscopy was also done for Chapter 2, however it became irrelevant in the data progression and is shown here. The figure demonstrates the effect of washing cycles on the acetate peaks and the effect of Citrate washing. All are found to be Calcium phosphates, however no significant structural features allowed it to be relevant.

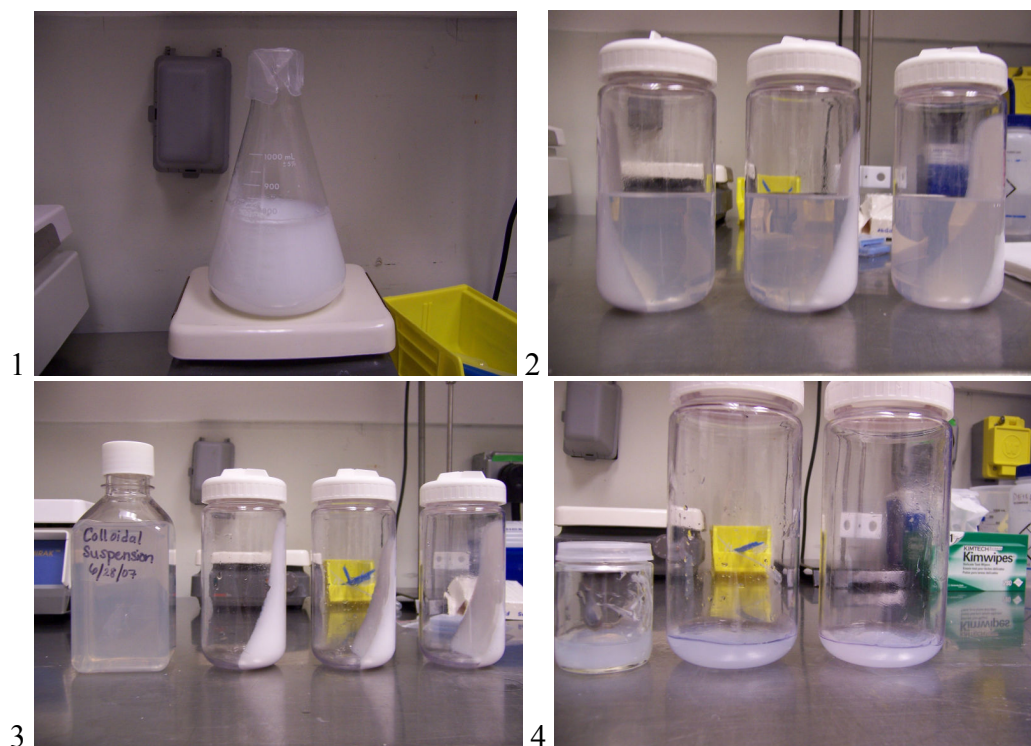


AP Figure 3. FTIR of hydroxyapatite powders produced in chapter 2

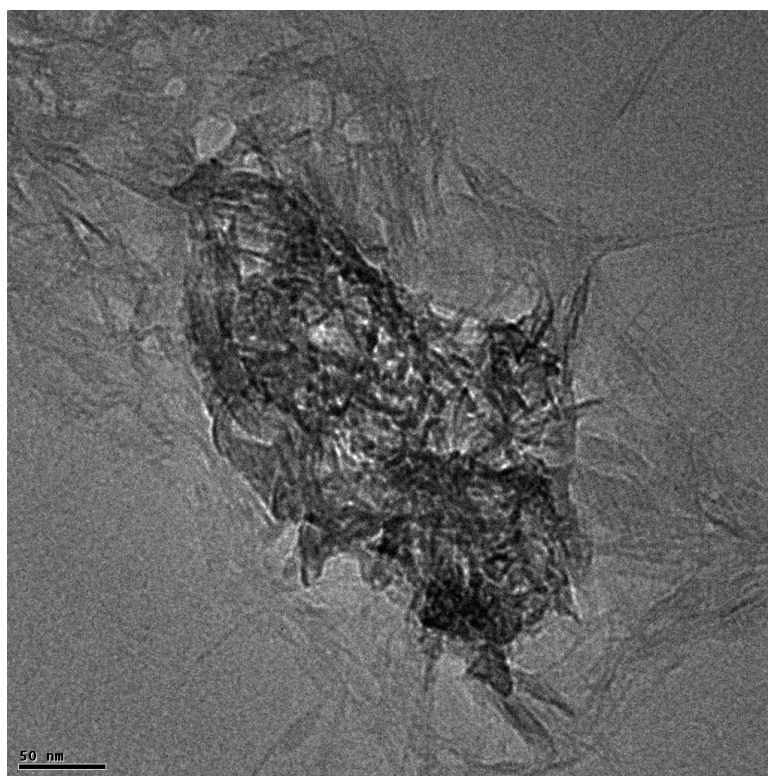
AP Table 1. FTIR peak references corresponding to AP Figure 3

Experimental Range	Band Assignment	Species	Literature Range
620-626	OH	HA	632
653-675	OCO δ	HA	550-1050
890-895	CO ₃ ν_2	HA	870
961-978	PO ₄ ν_1	HA	962
1022-1025	PO ₄ ν_3	HA	1032-1090
1425-1434	CH ₃ δ	[CH ₃ COO]	1429
1574-1594	COO ν_3	[CH ₃ COO]	1578
2500-3600	H ₂ O	N/A	2500-3600

Another two related side projects were briefly pursued for proof of concept. The first was a hydroxyapatite colloidal reeptization where a highly concentrated colloidal suspension of 50x5 nm rods are stabilized, even through water dilution or other methods typically thought to disrupt the electronic double layer. The procedure utilizes citrate washing, where following synthesis, the 0.2 M citric acid-ammonia neutralized wash media is added directly to the unwashed mother liquor. This is then allowed to stir overnight and is centrifuged the following day at 5000 rpm. The supernatant is poured off and the viscous mud-type material is allowed to sit in the centrifuge tube untouched for 3 days. This then appears to form a translucent colloidal gel, however with agitation immediately becomes a dense colloidal solution able to be diluted or freeze dried directly. Freezing was not observed to disrupt the structure, as with thawing at room temperature, it remained a colloidal suspension. Chronological procedure pictures are documented below in AP Figure 4. Particle size was estimated from HR TEM courtesy of UNM shown in AP Figure 5.



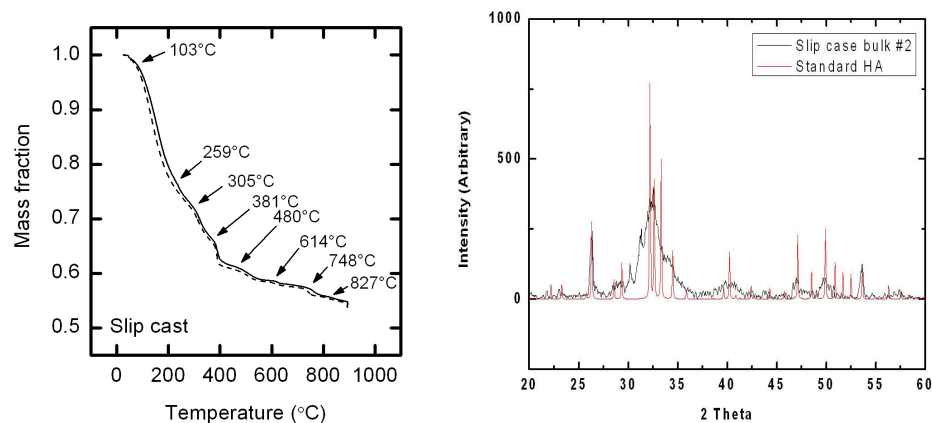
AP Figure 4. Chronological results of the colloidal reptization



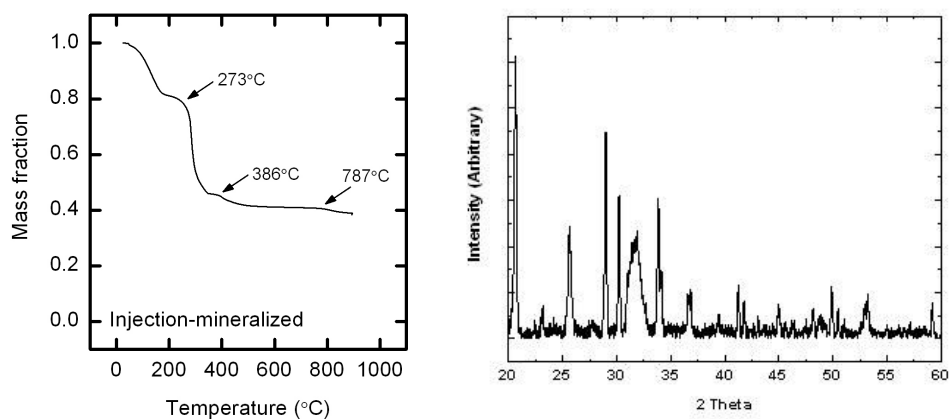
AP Figure 5. HR TEM of the colloidal suspension

The second additional project that was investigated was the slip casting and injection mineralization of allograft scaffolds in attempt to create load-bearing structures. Traditional slip casting methods were employed and preparation was as follows: about 5g of a demineralized fiber matrix were broken up in 50 mL of Calcium acetate stock solution, 50 mL of phosphate solution was then added and stirred, and this mixture was then poured into a plaster mold for compaction and dehydration over 5 days in a hood. Slip casting was successful in yielding inorganic mineral phases around 52% (AP Figure 6) through traditional methods where separated demineralized allograft fibers were mineralized then immediately slip cast. The XRD showed the dominant mineral phase was hydroxyapatite (AP Figure 6). Overall the injection of the mineral was also successful as numbers around 40% were recorded (AP Figure 7), however mechanical integrity fell below expectations for a load-bearing material. The alternating calcium and phosphate solution additions (~10 mL each time) were injected into multiple sites over the surface and interior of the mat (sitting on a Nalgene vacuum filter) in a grid fashion and the needle was gently removed. When the needle would no longer penetrate the surface the mat was flipped and the procedure was done on the other side. The mat was continually flipped until the mat was too dense on all sides to accept the needle. It was then stored in water until analysis or dried for TGA. The XRD revealed that hydroxyapatite was not the only phase precipitated within the structure when injection mineralized, monetite was also a significant phase co-precipitated. This stems from this specific procedure using a 2.0 M solution of Calcium acetate and a 1.2 M solution of potassium phosphate tribasic monohydrate neutralized to pH=7. This equal-volume precursor injection synthesis reaction creates a slurry with a pH of around 6, below the

metastable region of hydroxyapatite, prompting the co-precipitation of hydroxyapatite and monetite. This dual-precursor combination, however, is needed because the use of non-neutralized phosphate creates a gel, whereas this neutralized phosphate creates a thin slurry. To densely precipitate within the porous structure of an allograft, the thin solution is needed to maximize inorganic content. The synthesis precursor process lends well to injection mineralization (using 28 gauge insulin needles) due to both precursors being aqueous, likely making electrospinning or rapidprototyping an easy feat. The following figure shows a TGA analysis (performed by Anders Petersson) of the high mineral content materials.



AP Figure 6. TGA and XRD results of the slip cast sample showing about 52% mineral (hydroxyapatite) was successfully slipcast to make the composite.



AP Figure 7. TGA and XRD results of the injection mineralized sample showing about 40% mineral (hydroxyapatite and monetite) was successfully injected and remained within the sample.

Curriculum Vitae
Christina Marie Mossaad

Education:

- May '04 Clemson University, Clemson, SC
Ceramic & Materials Engineering
Bachelor of Science
- May '08 Rutgers University, Piscataway, NJ
Materials Science and Engineering
Master of Science
- January '09 Rutgers University, Piscataway, NJ
Materials Science and Engineering
Doctor of Philosophy

Principal Occupation:

Rutgers University Piscataway, NJ
May '04 – January '09
Graduate Research Assistant, NASA Fellow, IGERT Fellow